Four-Node Tetrahedral Elements for Gradient-Elasticity Analysis

K.Y.Sze[1*], W.C.Yuan[1], Y.X.Zhou[1,2]

[1]*Department of Mechanical Engineering, The University of Hong Kong, Pokfulam, Hong Kong, China.*
[2]*Faculty of Science, Harbin Institute of Technology (Shenzhen), Shenzhen, China.*
* Corresponding author (email: kysze@hku.hk)

Abstract

Computational analyses of gradient-elasticity often require the trial solution to be C^1 yet constructing simple C^1 finite elements is not trivial. Further to the recent success of devising 24-dof 4-node quadrilateral elements for 2D gradient-elasticity analyses, this paper develops two 48-dof 4-node tetrahedral elements for 3D gradient-elasticity analyses by generalizing the discrete Kirchhoff method and a relaxed hybrid-stress method. Displacement and displacement-gradient are the only nodal dofs. Both methods start with the derivation of a C^0 quadratic-complete displacement interpolation from which the strain is derived. In the first element, displacement-gradient at the mid-side points are approximated and interpolated together with those at the nodes whilst the strain-gradient is derived from the displacement-gradient interpolation. In the second element, the assumed constant double-stress modes are employed to enforce the continuity of the normal derivative of the displacement. The whole formulation can be viewed as if the strain-gradient matrix derived from the displacement interpolation matrix is refined by a constant matrix. Both elements are validated by the individual element patch test and other numerical benchmark tests. To the best knowledge of the authors, the proposed elements are probably the first non-mixed/penalty 3D elements which employ only engineering nodal dofs for gradient-elasticity analyses.

1. Introduction

In the conventional elasticity theory, strain is usually employed as the only deformation measure and the intrinsic length of the material does not present in the material parameters. It is suitable for applications when the characteristic length of the deformation is considerably larger than the intrinsic length. However, when the characteristic length is comparable to the intrinsic length such as in artificial cellular/foam materials and micro/nano-devices [1-6], size effect may arise and even dominate the deformation behaviour of structures. To take the size effect into account, various gradient-enhanced theories including but not restricted to non-local elasticity theory [7], strain-gradient theory [6] and couple-stress theory [8] have been proposed. A bottleneck for many gradient-enhanced theories to gain wider acceptance and applications is probably the C^1 requirement on the basis functions. While meshless and isogeometric methods can construct highly continuous basis functions [2, 9-15], special techniques are usually required to enforce the boundary conditions. Furthermore, the domains of influence of the highly continuous basis functions in these methods are larger, leading to less sparse system matrices and long computing time. Meanwhile, the Boundary Element Method (BEM) has been used successfully for gradient elasticity [16, 17]. To date, the finite element method (FEM) remains to be the most commonly-used tool for engineering analyses of solids and structures. Unfortunately, the existing C^1 finite element models pose strict requirement on the mesh topology [18-20] possess second/third order derivatives of the interpolated variable as the nodal dofs and/or employ heterosis nodes [21]. For instance, Agyris's 3-node and 6-node triangles use ($\mathbf{u}$, $\mathbf{u}_{,x}$, $\mathbf{u}_{,y}$, $\mathbf{u}_{,xx}$, $\mathbf{u}_{,xy}$, $\mathbf{u}_{,yy}$) and $\mathbf{u}_{,n}$, the displacement gradient along the outward normal direction, as the dofs at the corner and mid-side nodes, respectively [22]. Though the geometry requirement can be relaxed by using mapped meshes or smoothing the mesh, the former is restrictive and the latter requires special pre-processing treatment [18-20].

To circumvent the C^1 requirement, several non-conventional elements for gradient-enhanced theories have been developed in both 2D and 3D analyses. Zervos [23] introduced different 2D and 3D isoparametric elements. In his models, displacement and micro-deformation fields were interpolated independently. The penalty approach was used to enforce the kinematic constraint between the two fields. Zybell et al. [24] proposed a mixed brick element in which the kinematic constraint between displacement and gradients were enforced by the Lagrange multiplier method. Moreover, the discrete Kirchhoff (DK) method, which was first proposed for formulating thin-plate elements, has also been used to devise elements for strain-gradient/couple-stress theories [25, 26]. By using the DK method, kinematic constraints were enforced in a discrete manner. Recently, a 4-node quadrilateral DK4 element was devised for 2D strain-gradient problem [27]. Unlike the previous DK elements, the displacement and displacement-gradient interpolations in DK4 are closely related.

Besides, the 4-node quadrilateral relaxed-hybrid (RH4) element in reference [27] achieved the weak C^1 continuous requirement by using a variant of the refined direct stiffness method (RDSM) proposed for thin plate element formulation [26]. Instead of using a relaxed three-field hybrid functional for the variational justification in [26], RH4 uses a simpler two-field relaxed hybrid functional which is also simplified by invoking C^0 feature of the displacement interpolation. Both elements pass the constant double-stress patch test and are convergent in all numerical examples.

In this article, the formulations devised for the 2D elements DK4 and RH4 in reference [27] are extended to devise two 3D 4-node tetrahedral elements for strain-gradient elasticity analyses. Same as the 2D elements, the nodal dofs in the 3D elements include only the displacement $\mathbf{u}$ and the displacement gradients ($\mathbf{u}_{,x}$, $\mathbf{u}_{,y}$, $\mathbf{u}_{,z}$). In both elements, displacements along the six element edges are constructed by using the cubic Hermite interpolation. The C^0 displacement along the element edges is extended to the element domain by interpolating the displacements at the 4 nodes and 12 edge points. The interpolation functions are modified from those of the 20-node complete cubic tetrahedral element. In the first element DKT4 formulated by the generalized DK method, the displacement-gradient is interpolated by using the displacement gradients at the 4 nodes and 6 mid-edge points. The interpolation functions are the same as those of the 10-node complete cubic quadratic tetrahedral element. At the mid-edge point, the tangential displacement gradient is derived from the cubic Hermite interpolation of the displacement whilst the normal gradients are linearly interpolated from the two nodes defining the element edge. Strain and strain-gradient are derived from the displacement and displacement-gradient interpolations, respectively. In the second element RHT4 formulated by a relaxed-hybrid functional, both the strain and the strain-gradient are computed from the displacement interpolation. However, a refinement term arising from a relaxed-hybrid functional to the matrix relating the strain-gradient and the nodal dofs is incorporated for fulfilling the constant double-stress patch test. The method can be regarded as a variant of the refined direct stiffness method [27, 28] but the variational justification and the element formulation are simpler. The consistency of the two proposed elements is verified through the individual element test (IET) [29]. Both elements are validated by various numerical tests. To the best knowledge of the authors, the proposed elements are probably the first non-mixed/penalty 3D elements which employ only displacement and displacement-gradient as the nodal dofs for gradient-elasticity analyses.

2. Potential Energy Functional for 3D Gradient Elasticity

The potential energy functional and its variation for a plane element modelling the gradient elastic

material have been presented in [27]. Those for a 3D element domain Ω^e can be expressed as:

$$\Pi_P^e = \int_{\Omega^e} W(\varepsilon_{ij}, \kappa_{ijk}) d\Omega - P^e \quad \text{and} \quad \delta\Pi_P^e = \int_{\Omega^e} (\sigma_{ij}\delta\varepsilon_{ij} + m_{ijk}\delta\kappa_{ijk}) d\Omega - \delta P^e \tag{1a,b}$$

where W is the strain energy density function, ε_{ij} is the strain, κ_{ijk} is the strain-gradient, $\sigma_{ij} = \partial W/\partial\varepsilon_{ij}$ is the stress, $m_{ijk} = \partial W/\partial\kappa_{ijk}$ is the double-stress and P^e is the element load potential. Restricting ourselves to linear strain-gradient elasticity, and invoking the kinematic relations $\varepsilon_{ij} = (u_{i,j} + u_{j,i})/2$ and $\kappa_{ijk} = (u_{k,ij} + u_{j,ki})/2 = \varepsilon_{jk,i}$ in which u_i is the displacement, (1a,b) can be expressed in matrix-vector form as

$$\Pi_P^e = \frac{1}{2}\int_{\Omega^e} (\boldsymbol{\varepsilon}^T \mathbf{C}_\varepsilon \boldsymbol{\varepsilon} + \begin{Bmatrix} \boldsymbol{\varepsilon}_{,1} \\ \boldsymbol{\varepsilon}_{,2} \\ \boldsymbol{\varepsilon}_{,3} \end{Bmatrix}^T \mathbf{C}_g \begin{Bmatrix} \boldsymbol{\varepsilon}_{,1} \\ \boldsymbol{\varepsilon}_{,2} \\ \boldsymbol{\varepsilon}_{,3} \end{Bmatrix}) d\Omega - P^e, \quad \delta\Pi_P^e = \int_{\Omega^e} \boldsymbol{\sigma}^T(\mathbf{L}\delta\mathbf{u}) + \begin{Bmatrix} \mathbf{m}^1 \\ \mathbf{m}^2 \\ \mathbf{m}^3 \end{Bmatrix}^T \begin{bmatrix} \mathbf{L}\delta\mathbf{u}_{,1} \\ \mathbf{L}\delta\mathbf{u}_{,2} \\ \mathbf{L}\delta\mathbf{u}_{,3} \end{bmatrix}] d\Omega - \delta P^e \tag{2a,b}$$

in which

$$\mathbf{u} = \begin{Bmatrix} u_1 \\ u_2 \\ u_3 \end{Bmatrix}, \quad \boldsymbol{\varepsilon} = \begin{Bmatrix} \varepsilon_{11} \\ \varepsilon_{22} \\ \varepsilon_{33} \\ 2\varepsilon_{23}(=2\varepsilon_{32}) \\ 2\varepsilon_{31}(=2\varepsilon_{31}) \\ 2\varepsilon_{12}(=2\varepsilon_{21}) \end{Bmatrix} = \mathbf{L}\mathbf{u}, \quad \mathbf{L} = \begin{bmatrix} \partial/\partial x_1 & 0 & 0 \\ 0 & \partial/\partial x_2 & 0 \\ 0 & 0 & \partial/\partial x_3 \\ 0 & \partial/\partial x_3 & \partial/\partial x_2 \\ \partial/\partial x_3 & 0 & \partial/\partial x_1 \\ \partial/\partial x_2 & \partial/\partial x_1 & 0 \end{bmatrix}, \quad \boldsymbol{\sigma} = \mathbf{C}_\varepsilon\boldsymbol{\varepsilon} \text{ and } \begin{Bmatrix} \mathbf{m}^1 \\ \mathbf{m}^2 \\ \mathbf{m}^3 \end{Bmatrix} = \mathbf{C}_g \begin{Bmatrix} \boldsymbol{\varepsilon}_{,1} \\ \boldsymbol{\varepsilon}_{,2} \\ \boldsymbol{\varepsilon}_{,2} \end{Bmatrix}$$

are the displacement vector, vector of strain components, strain-displacement operator, vector of stress components and vector of double-stress components, respectively. Moreover, $\mathbf{C}_\varepsilon$ and $\mathbf{C}_g$ are the material matrices and $\mathbf{m}^i = \{m_{i11}, m_{i22}, m_{i33}, m_{i23}(=m_{i32}), m_{i13}(=m_{i31}), m_{i12}(=m_{i21})\}^T$. For instance, a simple form of gradient-elasticity adopts $\mathbf{C}_g = l^2 diag.\{\mathbf{C}_\varepsilon, \mathbf{C}_\varepsilon, \mathbf{C}_\varepsilon\}$ in which l is intrinsic length of the material. Using the divergence theorem, (2b) can be expressed as

$$\delta\Pi_P^e = -\int_{\Omega^e} [\mathbf{L}^T(\boldsymbol{\sigma} - \mathbf{m}^1{}_{,1} - \mathbf{m}^2{}_{,2} - \mathbf{m}^3{}_{,3})]^T \delta\mathbf{u}\, d\Omega$$

$$+ \int_{\partial\Omega^e} \left([\mathbf{v}(n)(\boldsymbol{\sigma} - \mathbf{m}^1{}_{,1} - \mathbf{m}^2{}_{,2} - \mathbf{m}^3{}_{,3})]^T \delta\mathbf{u} + (n_1\mathbf{m}^1 + n_2\mathbf{m}^2 + n_3\mathbf{m}^2)^T(\mathbf{L}\delta\mathbf{u}) \right) d\Gamma - \delta P^e \tag{3}$$

where $\mathbf{e}_n = \{n_i\}$ is the unit outward normal vector to the element boundary $\partial\Omega^e$ and

$$\mathbf{v}(n) = \begin{bmatrix} n_1 & 0 & 0 & 0 & n_3 & n_2 \\ 0 & n_2 & 0 & n_3 & 0 & n_1 \\ 0 & 0 & n_3 & n_2 & n_1 & 0 \end{bmatrix}.$$

By decomposing the gradient of the virtual displacement into surface and normal gradients, the

boundary integral in (3) for elements defined by planar boundary facets can be expressed as [19, 30]:

$$\int_{\partial \Omega^e} (\mathbf{t}^T \delta \mathbf{u} + \boldsymbol{\mu}^T \delta \mathbf{u},_n) d\Gamma \tag{4}$$

where $\mathbf{t} = \{t_i\}$ is the traction, $\boldsymbol{\mu} = \{\mu_i\}$ is the double-traction, $t_k = n_j(\sigma_{jk} - m_{ijk,i}) - n_i(\delta_{jl} - n_j n_l) m_{ijk,l}$,

$\mu_k = n_i n_j m_{ijk}$ and $\mathbf{u},_n$ is the normal gradient of the displacement. Thus, the element load potential is

$$P^e = \int_{\Gamma_t^e} \overline{\mathbf{t}}^T \mathbf{u} d\Gamma + \int_{\Gamma_\mu^e} \overline{\boldsymbol{\mu}}^T \mathbf{u},_n d\Gamma \tag{5}$$

in which $\overline{\mathbf{t}}$ and $\overline{\boldsymbol{\mu}}$ are the prescribed traction and double-traction over the portions Γ_t^e and Γ_μ^e of $\partial\Omega^e$, respectively. It can be seen in (4) that $\mathbf{u}$ and $\mathbf{u},_n$ need to be C^0 at the inter-element boundary for enforcing the reciprocities of $\mathbf{t}$ and $\boldsymbol{\mu}$, respectively. In other words, $\mathbf{u}$ is required to be C^1.

3. C^0 Displacement Interpolation

In this section, a C^0 quadratic-complete displacement interpolation will be derived for the two 48-dof 4-node tetrahedral elements. The C^1 requirement on the displacement will be dealt with in the next two sections. The 12 nodal dofs of the element are $\mathbf{u}$, $\mathbf{u},_1$, $\mathbf{u},_2$ and $\mathbf{u},_3$ in which $\mathbf{u}$ is the displacement vectors and the others form the displacement-gradient with respect to the global Cartesian coordinates (x_1, x_2, x_3).

3.1 Interpolation Functions for the 16-node Tetrahedron

Figure 1(a) shows the 20-node tetrahedron in its volumetric coordinates ξ_1, ξ_2, $\xi_3 \in [0,1]$. The interpolation basis is complete in the third order. With respect to the node numbering scheme, the interpolation functions can be expressed as

$$\widehat{N}_1 = \frac{1}{2}\xi_2\eta_2(\eta_2 - 1), \ \widehat{N}_2 = \frac{1}{2}\xi_3\eta_3(\eta_3 - 1), \ \widehat{N}_3 = \frac{1}{2}\xi_4\eta_4(\eta_4 - 1), \ \widehat{N}_4 = \frac{1}{2}\xi_1\eta_1(\eta_1 - 1),$$

$$\widehat{N}_5 = \frac{9}{2}\xi_2\xi_3\eta_2, \widehat{N}_6 = \frac{9}{2}\xi_2\xi_3\eta_3, \ \widehat{N}_7 = \frac{9}{2}\xi_3\xi_4\eta_3, \widehat{N}_8 = \frac{9}{2}\xi_3\xi_4\eta_4, \ \widehat{N}_9 = \frac{9}{2}\xi_2\xi_4\eta_4, \widehat{N}_{10} = \frac{9}{2}\xi_2\xi_4\eta_2,$$

$$\widehat{N}_{11} = \frac{9}{2}\xi_1\xi_2\eta_2, \widehat{N}_{12} = \frac{9}{2}\xi_3\xi_1\eta_3, \ \widehat{N}_{13} = \xi_4\xi_1\eta_4, \widehat{N}_{14} = \frac{9}{2}\xi_1\xi_2\eta_1, \ \widehat{N}_{15} = \frac{9}{2}\xi_3\xi_1\eta_1, \widehat{N}_{16} = \frac{9}{2}\xi_4\xi_1\eta_1,$$

$$\widehat{N}_{17} = 27\xi_2\xi_3\xi_4, \widehat{N}_{18} = 27\xi_1\xi_2\xi_3, \ \widehat{N}_{19} = 27\xi_3\xi_4\xi_1, \widehat{N}_{20} = 27\xi_4\xi_1\xi_2 \tag{6}$$

where $\xi_4 = 1 - \xi_1 - \xi_2 - \xi_3$ and $\eta_i = 3\xi_i - 1$. In the absence of node 17 to node 20 which are face bubble nodes, the 20-node element reduces to the 16-node element, see Figure 1(b). By cyclic symmetry, the reduction allows the interpolation functions N_1 to N_{16} of the 16-node tetrahedron to be expressed as:

$$\begin{Bmatrix} N_{14} \\ N_{11} \end{Bmatrix} = \begin{Bmatrix} \hat{N}_{14} \\ \hat{N}_{11} \end{Bmatrix} + b \begin{Bmatrix} \hat{N}_{20} + \hat{N}_{18} \\ \hat{N}_{20} + \hat{N}_{18} \end{Bmatrix}, \quad \begin{Bmatrix} N_5 \\ N_6 \end{Bmatrix} = \begin{Bmatrix} \hat{N}_5 \\ \hat{N}_6 \end{Bmatrix} + b \begin{Bmatrix} \hat{N}_{17} + \hat{N}_{18} \\ \hat{N}_{17} + \hat{N}_{18} \end{Bmatrix}, \quad \begin{Bmatrix} N_{12} \\ N_{15} \end{Bmatrix} = \begin{Bmatrix} \hat{N}_{12} \\ \hat{N}_{15} \end{Bmatrix} + b \begin{Bmatrix} \hat{N}_{18} + \hat{N}_{19} \\ \hat{N}_{18} + \hat{N}_{19} \end{Bmatrix},$$

$$\begin{Bmatrix} N_{16} \\ N_{13} \end{Bmatrix} = \begin{Bmatrix} \hat{N}_{16} \\ \hat{N}_{13} \end{Bmatrix} + b \begin{Bmatrix} \hat{N}_{19} + \hat{N}_{20} \\ \hat{N}_{19} + \hat{N}_{20} \end{Bmatrix}, \quad \begin{Bmatrix} N_{10} \\ N_9 \end{Bmatrix} = \begin{Bmatrix} \hat{N}_{10} \\ \hat{N}_9 \end{Bmatrix} + b \begin{Bmatrix} \hat{N}_{17} + \hat{N}_{20} \\ \hat{N}_{17} + \hat{N}_{20} \end{Bmatrix}, \quad \begin{Bmatrix} N_7 \\ N_8 \end{Bmatrix} = \begin{Bmatrix} \hat{N}_7 \\ \hat{N}_8 \end{Bmatrix} + b \begin{Bmatrix} \hat{N}_{17} + \hat{N}_{19} \\ \hat{N}_{17} + \hat{N}_{19} \end{Bmatrix},$$

$$N_1 = \hat{N}_1 + a(\hat{N}_{20} + \hat{N}_{17} + \hat{N}_{18}), \quad N_2 = \hat{N}_2 + a(\hat{N}_{17} + \hat{N}_{18} + \hat{N}_{19}),$$

$$N_3 = \hat{N}_3 + a(\hat{N}_{17} + \hat{N}_{19} + \hat{N}_{20}), \quad N_4 = \hat{N}_4 + a(\hat{N}_{19} + \hat{N}_{20} + \hat{N}_{18}). \tag{7}$$

The Kronecker delta property of the interpolation functions leads to two independent equations on a and b which are solved to be

$$a = -9/2 \quad \text{and} \quad b = 27/4. \tag{8}$$

It is trivial that the interpolation basis is quadratic-complete with some incomplete cubic terms.
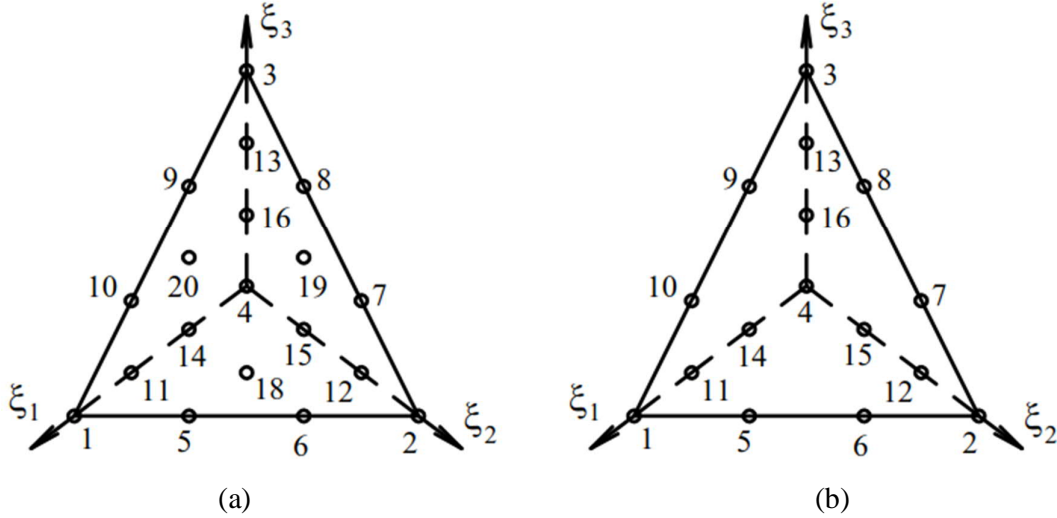
Figure 1. (a) The 20-node tetrahedron, node 17 which is not shown is at the centroid of the face defined by nodes 1, 2 and 3. (b) The 16-node tetrahedron. $\xi_1, \xi_2, \xi_3 \in [0,1]$ are the volume coordinates.

For clarity, the edge nodes will be termed as edge points and the corner nodes will simply be termed as nodes from here onwards. The edge points do not possess its own independent dofs.

3.2 Displacement at Edge Points

Figure 2 shows an arbitrary element edge bounded by nodes i and j whilst p and q are the edge-

points equally divide the straight edge into three segments. Furthermore, s is the running coordinate from node i to node j. Using the Hermite interpolation, the displacement $\mathbf{u}$ along the edge in terms of the nodal dofs at i and j is

$$\mathbf{u} = (\frac{2s}{L}+1)(\frac{s}{L}-1)^2 \mathbf{u}_i + s(1-\frac{s}{L})^2 (\mathbf{u},_s)_i + (\frac{s}{L})^2 (3-\frac{2s}{L})\mathbf{u}_j + \frac{s^2}{L}(\frac{s}{L}-1)(\mathbf{u},_s)_j . \qquad (9)$$

where $L = |\mathbf{x}_j - \mathbf{x}_i|$ is the length of the element edge. Thus, the displacements at points p and q are

$$\begin{Bmatrix} \mathbf{u}_p \\ \mathbf{u}_q \end{Bmatrix} = \begin{Bmatrix} \mathbf{u}\,|_{s=L/3} \\ \mathbf{u}\,|_{s=2L/3} \end{Bmatrix} = \frac{1}{27}(\mathbf{u}_i \begin{Bmatrix} 20 \\ 7 \end{Bmatrix} + \mathbf{u}_j \begin{Bmatrix} 7 \\ 20 \end{Bmatrix} + (\mathbf{u},_s)_i \begin{Bmatrix} 4 \\ 2 \end{Bmatrix} - (\mathbf{u},_s)_j \begin{Bmatrix} 2 \\ 4 \end{Bmatrix}) . \qquad (10)$$
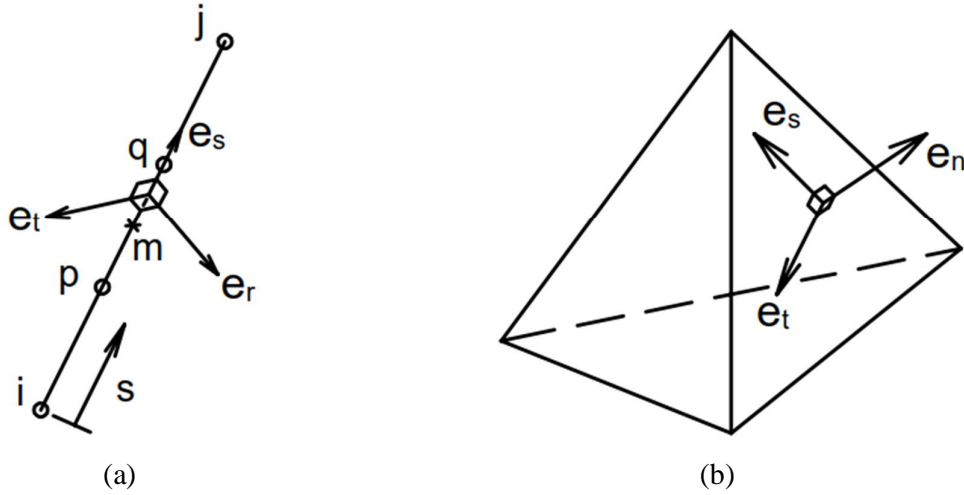

(a)   (b)

Figure 2. (a) An element edge bounded by nodes i and j; p and q are the edge points dividing the edge into three equal segments; m is the mid-edge point; $(\mathbf{e}_r, \mathbf{e}_s, \mathbf{e}_t)$ is a local orthogonal triad of the element edge. (b) A local orthogonal triad $(\mathbf{e}_n, \mathbf{e}_s, \mathbf{e}_t)$ of an element face; $\mathbf{e}_n$ is normal to the element face.

On the other hand, $\mathbf{u},_s$ can be derived from the displacement-gradient through

$$\mathbf{u},_s = \frac{\partial x_1}{\partial s}\mathbf{u},_1 + \frac{\partial x_2}{\partial s}\mathbf{u},_2 + \frac{\partial x_3}{\partial s}\mathbf{u},_3 = s_1\mathbf{u},_1 + s_2\mathbf{u},_2 + s_3\mathbf{u},_3 \qquad (11)$$

where s_i is the component of the unit vector $\mathbf{e}_s = \{s_i\} = \frac{1}{L}(\mathbf{x}_j - \mathbf{x}_i)$.

3.3 Displacement inside the Element

From (9), (10) and (11), the displacements at all the 12 edge points in Figure 1(b) can be determined in terms of the nodal dofs. They together with the 4 nodal displacements are interpolated using the interpolation functions derived for the 16-node tetrahedron, see (7) and (8). The resulting

C^0 displacement would be expressed symbolically as

$$\mathbf{u} = \mathbf{Nd} = \mathbf{N} \begin{Bmatrix} \mathbf{d}_1 \\ \mathbf{d}_2 \\ \mathbf{d}_3 \\ \mathbf{d}_4 \end{Bmatrix} \quad \text{and} \quad \mathbf{d}_i = \begin{Bmatrix} (\mathbf{u})_i \\ (\mathbf{u}_{,1})_i \\ (\mathbf{u}_{,2})_i \\ (\mathbf{u}_{,3})_i \end{Bmatrix} \tag{12}$$

where $\mathbf{N}$ is the displacement interpolation matrix, $\mathbf{d}$ is the element vector of nodal dofs and $(\ )_i$ denotes the parenthesized vector at the i-th node.

4. The Generalized Discrete Kirchhoff Element

Thin plate bending is perhaps the most well-known problem that imposes the C^1 requirement in the trial function space. Among the commonly used finite element methods for thin plate analyses, the DK method offers a simple and high practicable approach for element formulation that can avoid the C^1 interpolation [31-33] and secure the constant moment patch test. In the method, the nodal dofs are the transverse deflection and the rotation of the director. By imposing the Kirchhoff constraint at the nodes, the third order Hermite interpolation for the deflection can be constructed along each edge. The mid-edge director rotation about the edge normal is derived from the interpolation and the Kirchhoff constraint. The mid-edge director rotation about edge tangent is linearly interpolated from the two end nodes defining the edge. The director rotation field from which the curvature can be derived is then interpolated using the rotation of the director at the nodes and the mid-edge points. The DK method has been generalized to derive 4-node quadrilateral elements for plane gradient elasticity [25-27]. In this section, it will be generalized to derive the displacement-gradient for the 4-node tetrahedral element for 3D gradient-elasticity analyses.

4.1 Displacement Gradient at Mid-Edge Points

Figure 2(a) also shows the mid-edge point m and the orthogonal triad formed by unit vectors $\mathbf{e}_r = \{r_i\}$, $\mathbf{e}_s = \{s_i\}$ and $\mathbf{e}_t = \{t_i\}$. Further to (11), displacement derivatives with respect to (x_1, x_2, x_3) and (r,s,t) are related through

$$\begin{Bmatrix} \mathbf{u}_{,r} \\ \mathbf{u}_{,s} \\ \mathbf{u}_{,t} \end{Bmatrix} = \begin{bmatrix} r_1\mathbf{I}_3 & r_2\mathbf{I}_3 & r_3\mathbf{I}_3 \\ s_1\mathbf{I}_3 & s_2\mathbf{I}_3 & s_3\mathbf{I}_3 \\ t_1\mathbf{I}_3 & t_2\mathbf{I}_3 & t_3\mathbf{I}_3 \end{bmatrix} \begin{Bmatrix} \mathbf{u}_{,1} \\ \mathbf{u}_{,2} \\ \mathbf{u}_{,3} \end{Bmatrix} \quad \text{and} \quad \begin{Bmatrix} \mathbf{u}_{,1} \\ \mathbf{u}_{,2} \\ \mathbf{u}_{,3} \end{Bmatrix} = \begin{bmatrix} r_1\mathbf{I}_3 & r_2\mathbf{I}_3 & r_3\mathbf{I}_3 \\ s_1\mathbf{I}_3 & s_2\mathbf{I}_3 & s_3\mathbf{I}_3 \\ t_1\mathbf{I}_3 & t_2\mathbf{I}_3 & t_3\mathbf{I}_3 \end{bmatrix}^T \begin{Bmatrix} \mathbf{u}_{,r} \\ \mathbf{u}_{,s} \\ \mathbf{u}_{,t} \end{Bmatrix} \tag{13a,b}$$

Following the idea of the discrete Kirchhoff element, $\mathbf{u}_{,s}$ at m is derived from (9) and (13a) as

$$(\mathbf{u}_{,s})_m = \frac{3}{2L}(\mathbf{u}_j - \mathbf{u}_i) - \frac{S_1}{4}\big((\mathbf{u}_{,1})_i + (\mathbf{u}_{,1})_j\big) - \frac{S_2}{4}\big((\mathbf{u}_{,2})_i + (\mathbf{u}_{,2})_j\big) - \frac{S_3}{4}\big((\mathbf{u}_{,3})_i + (\mathbf{u}_{,3})_j\big) \qquad (14)$$

whilst the other two displacement derivatives are linearly interpolated at nodes i and j, i.e.

$$(\mathbf{u}_{,r})_m = \frac{1}{2}\big((\mathbf{u}_{,r})_i + (\mathbf{u}_{,r})_j\big) = \frac{1}{2}\big(r_1((\mathbf{u}_{,1})_i + (\mathbf{u}_{,1})_j) + r_2((\mathbf{u}_{,2})_i + (\mathbf{u}_{,2})_j) + r_3((\mathbf{u}_{,3})_i + (\mathbf{u}_{,3})_j)\big) ,$$

$$(\mathbf{u}_{,t})_m = \frac{1}{2}\big((\mathbf{u}_{,t})_i + (\mathbf{u}_{,t})_j\big) = \frac{1}{2}\big(t_1((\mathbf{u}_{,1})_i + (\mathbf{u}_{,1})_j) + t_2((\mathbf{u}_{,2})_i + (\mathbf{u}_{,2})_j) + t_3((\mathbf{u}_{,3})_i + (\mathbf{u}_{,3})_j)\big). \qquad (15\text{a,b})$$

Using (14), (15) and (13b), the displacement-gradient $[\mathbf{u}_{,1}\ \mathbf{u}_{,2}\ \mathbf{u}_{,3}]$ at point m can be derived in terms of the dofs at nodes i and j. It can be easily shown that the derived $(\mathbf{u}_{,1})_m$ $(\mathbf{u}_{,2})_m$ and $(\mathbf{u}_{,3})_m$ are independent of the choices of $\mathbf{e}_r$ and $\mathbf{e}_t$. Similarly, the displacement-derivatives with respect to (x_1, x_2, x_3) at other mid-edge points can be derived in terms of the nodal dofs.

4.2 Interpolated Displacement-Gradient

The displacement-gradient at the four nodes and six mid-edge points can be interpolated by using the interpolation functions of the commonly used complete quadratic ten-node tetrahedron. Symbolically, the displacement-derivatives can be expressed as

$$\mathbf{u}_{,1} \simeq \phi^1 = \mathbf{N}_1\mathbf{d} , \quad \mathbf{u}_{,2} \simeq \phi^2 = \mathbf{N}_2\mathbf{d}, \quad \mathbf{u}_{,3} \simeq \phi^3 = \mathbf{N}_3\mathbf{d} \qquad (16)$$

which are denoted as ϕ^1, ϕ^2 and ϕ^3 to emphasis that they are not compatible to the interpolated-displacement in (12). Since $(\mathbf{u}_{,r})_m$ and $(\mathbf{u}_{,t})_m$ in (15) are exact for linear displacement-gradient, the interpolated displacement gradient $[\phi^1, \phi^2, \phi^3]$ is also exact for liner displacement-gradient.

4.3 Element Formulation

With $\mathbf{u}_{,1} = \phi^1$, $\mathbf{u}_{,2} = \phi^2$ and $\mathbf{u}_{,3} = \phi^3$ approximately satisfied, $\mathbf{u}_{,1}$, $\mathbf{u}_{,2}$ and $\mathbf{u}_{,3}$ are replaced by ϕ^1, ϕ^2 and ϕ^3, respectively, in computing the strain-gradient in (2a), which becomes

$$\Pi_{DK}^e = \frac{1}{2}\int_{\Omega^e}\left[(\mathbf{Lu})^T\mathbf{C}_\varepsilon(\mathbf{Lu}) + \begin{Bmatrix}\mathbf{L}\phi^1\\\mathbf{L}\phi^2\\\mathbf{L}\phi^3\end{Bmatrix}\mathbf{C}_g\begin{Bmatrix}\mathbf{L}\phi^1\\\mathbf{L}\phi^2\\\mathbf{L}\phi^3\end{Bmatrix}\right)d\Omega - P^e = \frac{1}{2}\mathbf{d}^T\mathbf{k}_{DKT4}\mathbf{d} - P^e. \qquad (17)$$

Thus, the C^1 requirement on $\mathbf{u}$ becomes the C^0 requirement on ϕ^1, ϕ^2 and ϕ^3. By incorporating the interpolations in (12) and (16),

$$\Pi_{DK}^e = \frac{1}{2}\mathbf{d}^T \int_{\Omega^e} [(\mathbf{LN}^T \mathbf{C}_\varepsilon (\mathbf{LN}) + \begin{bmatrix} \mathbf{LN}_1 \\ \mathbf{LN}_2 \\ \mathbf{LN}_3 \end{bmatrix}^T \mathbf{C}_g \begin{bmatrix} \mathbf{LN}_1 \\ \mathbf{LN}_2 \\ \mathbf{LN}_3 \end{bmatrix}]d\Omega \cdot \mathbf{d} - P^e = \frac{1}{2}\mathbf{d}^T \mathbf{k}_{DK}\mathbf{d} - P^e \tag{18}$$

in which the element stiffness matrix $\mathbf{k}_{DK}$ of the generalized Discrete Kirchhoff element DKT4 arising from the integration is self-defined. For the element, the strain-displacement matrix is $\mathbf{LN}$ and the strain-gradient-displacement matrix is $[(\mathbf{LN}_1)^T \ (\mathbf{LN}_2)^T \ (\mathbf{LN}_3)^T]^T$.

4.4 Generalized Individual Element Patch Test

The consistency of the generalized DK element can be verified by the individual element test (IET) which was proposed by Bergan and Hanssen in late 1970's [34] with the underlying goal to establish a test for element design. IET demands pairwise cancellation of tractions among adjacent elements under the same uniform stress state. It has been shown that the satisfaction of IET plus the proper rankness of the element stiffness matrix can secure the Forms A, B and C patch tests [29].

In the present strain gradient elasticity, a quadratic displacement $\mathbf{u}_Q$ leading to equilibrating stress and double-stress is considered, i.e.

$$\mathbf{L}^T(\boldsymbol{\sigma}_Q - \mathbf{m}_Q^1,_1 - \mathbf{m}_Q^2,_2 - \mathbf{m}_Q^2,_3) = \mathbf{L}^T \boldsymbol{\sigma}_Q = \mathbf{0} \tag{19}$$

in which

$$\boldsymbol{\sigma}_Q = \mathbf{C}_\varepsilon (\mathbf{Lu}_Q) \quad \text{and} \quad \begin{Bmatrix} \mathbf{m}_Q^1 \\ \mathbf{m}_Q^2 \\ \mathbf{m}_Q^3 \end{Bmatrix} = \mathbf{C}_g \begin{Bmatrix} (\mathbf{Lu}_Q),_1 \\ (\mathbf{Lu}_Q),_2 \\ (\mathbf{Lu}_Q),_3 \end{Bmatrix}$$

are linear in (x_1, x_2, x_3) and constant, respectively. Let $\mathbf{d}_Q$ be the element displacement vector prescribed according to $\mathbf{u}_Q$, $\mathbf{u}_Q,_1$, $\mathbf{u}_Q,_2$ and $\mathbf{u}_Q,_3$. Since $\mathbf{N}$ in (12) can reproduce the quadratic $\mathbf{u}_Q$ whilst $\mathbf{N}^1$, $\mathbf{N}^2$ and $\mathbf{N}^3$ in (16) can reproduce the linear $\mathbf{u}_Q,_1$, $\mathbf{u}_Q,_2$ and $\mathbf{u}_Q,_3$,

$$\mathbf{k}_{DK}\mathbf{d}_Q = \int_{\Omega^e} [(\mathbf{LN})^T \boldsymbol{\sigma}_Q + \begin{Bmatrix} \mathbf{LN}^1 \\ \mathbf{LN}^2 \\ \mathbf{LN}^3 \end{Bmatrix}^T \begin{Bmatrix} \mathbf{m}_Q^1 \\ \mathbf{m}_Q^2 \\ \mathbf{m}_Q^3 \end{Bmatrix}]d\Omega$$

$$= \int_{\partial\Omega^e} [\mathbf{N}^T \boldsymbol{\upsilon}(n)\boldsymbol{\sigma}_Q + (\mathbf{N}^1)^T \boldsymbol{\upsilon}(n)\mathbf{m}_Q^1 + (\mathbf{N}^2)^T \boldsymbol{\upsilon}(n)\mathbf{m}_Q^2 + (\mathbf{N}^3)^T \boldsymbol{\upsilon}(n)\mathbf{m}_Q^3]dS \cdot \tag{20}$$

In the above manipulation, no domain integrand is left after the integration by parts due to (19) and the constant nature of the double-stress. It should also be remarked that the transformation from

domain to boundary integral is analytical. When numerical integration is used, the domain integration rules must be able to evaluate the integrals exactly. For the present element, one must use at least the 5-point and 4-point integration rules for the domain integrals involving $\boldsymbol{\sigma}_Q$ and $(\mathbf{m}_Q^1, \mathbf{m}_Q^2, \mathbf{m}_Q^3)$, respectively.

Using the derived $\mathbf{N}$, $\mathbf{N}^1$, $\mathbf{N}^2$ and $\mathbf{N}^3$, the interpolated $\mathbf{u}$, $\boldsymbol{\phi}^1$, $\boldsymbol{\phi}^2$ and $\boldsymbol{\phi}^3$ along an element edge depend only on the dofs of the nodes along the same element edge, pairwise cancellation of the generalized boundary forces occur when (20) is assembled into the global equation. As far as the employed integration rule for evaluating $\mathbf{k}_{RH}$ satisfies the orders in the last paragraph and leads to a rank sufficient $\mathbf{k}_{RH}$, the element passes IET and, thus, the generalized patch test. Interested readers may consult Reference [29] for further details of the IET.

5. The Relaxed-Hybrid Element

In the section, a relaxed hybrid variation functional which contains independent domain displacement, boundary displacement and stress for conventional elasticity is first reviewed for completeness.

5.1 The Relaxed Hybrid Functional for Conventional Elasticity

For conventional elasticity, the elementwise Hellinger-Reissner functional and its variation [35] with independently assumed stress $\hat{\boldsymbol{\sigma}}$ and assumed compatible displacement $\mathbf{u}$ are:

$$\Pi_{HR}^e = \int_{\Omega^e} [-\frac{1}{2}\hat{\boldsymbol{\sigma}}^T \mathbf{C}_\varepsilon^{-1}\hat{\boldsymbol{\sigma}} + \hat{\boldsymbol{\sigma}}^T (\mathbf{Lu})]d\Omega - P^e \tag{21}$$

If the displacement is not compatible, an independently assumed boundary compatible displacement $\tilde{\mathbf{u}}$ can be introduced to form the following functional:

$$\Pi^e = \int_{\Omega^e} [-\frac{1}{2}\hat{\boldsymbol{\sigma}}^T \mathbf{C}_\varepsilon^{-1}\hat{\boldsymbol{\sigma}} + \hat{\boldsymbol{\sigma}}^T (\mathbf{Lu})]d\Omega - \int_{\partial\Omega^e} \left(\boldsymbol{\upsilon}(n)\hat{\boldsymbol{\sigma}}\right)^T (\mathbf{u} - \tilde{\mathbf{u}})dS - P^e \tag{22}$$

and its variation is

$$\delta\Pi^e = \int_{\Omega^e} [\delta\hat{\boldsymbol{\sigma}}^T (\mathbf{Lu} - \mathbf{C}_\varepsilon^{-1}\hat{\boldsymbol{\sigma}}) - \delta\mathbf{u}^T (\mathbf{L}^T\hat{\boldsymbol{\sigma}})]d\Omega - \int_{\partial\Omega^e} \left(\boldsymbol{\upsilon}(n)\delta\hat{\boldsymbol{\sigma}}\right)^T (\mathbf{u} - \tilde{\mathbf{u}})dS + \int_{\partial\Omega^e} \left(\boldsymbol{\upsilon}(n)\hat{\boldsymbol{\sigma}}\right)^T \delta\tilde{\mathbf{u}}dS - \delta P^e$$

$$\tag{23}$$

which enforces the strain compatibility, stress equilibrium, the equality of $\mathbf{u}$ and $\tilde{\mathbf{u}}$ as well as the

traction reciprocity in a weak sense. In the formulation, the assumed $\widehat{\boldsymbol{\sigma}}$ can be divided into constant modes $\widehat{\boldsymbol{\sigma}}_c$ and non-constant modes $\widehat{\boldsymbol{\sigma}}_n$. With the patch test fulfilment unaffected, enforcement of the traction reciprocity can be relaxed by using only $\widehat{\boldsymbol{\sigma}}_c$ in the boundary integral term in (22), i.e.,

$$\Pi^e = \int_{\Omega^e} [-\frac{1}{2}\widehat{\boldsymbol{\sigma}}^T \mathbf{C}^{-1}\widehat{\boldsymbol{\sigma}} + \widehat{\boldsymbol{\sigma}}^T(\mathbf{Lu})]d\Omega - \int_{\partial\Omega^e} \left(\upsilon(n)\widehat{\boldsymbol{\sigma}}_c\right)^T (\mathbf{u}-\tilde{\mathbf{u}})dS - P^e . \tag{24}$$

5.2 The Relaxed Hybrid Functional for Gradient Elasticity

By introducing independently assumed double-stress components $\widehat{\mathbf{m}}^1$, $\widehat{\mathbf{m}}^2$ and $\widehat{\mathbf{m}}^3$ into the potential energy functional given in (2) for gradient elasticity, we have

$$\Pi^e = \int_{\Omega^e} (\frac{1}{2}(\mathbf{Lu})^T \mathbf{C}_\varepsilon (\mathbf{Lu}) - \frac{1}{2}\begin{Bmatrix} \widehat{\mathbf{m}}^1 \\ \widehat{\mathbf{m}}^2 \\ \widehat{\mathbf{m}}^3 \end{Bmatrix}^T \mathbf{C}_g^{-1} \begin{Bmatrix} \widehat{\mathbf{m}}^1 \\ \widehat{\mathbf{m}}^2 \\ \widehat{\mathbf{m}}^3 \end{Bmatrix} + \begin{Bmatrix} \widehat{\mathbf{m}}^1 \\ \widehat{\mathbf{m}}^2 \\ \widehat{\mathbf{m}}^3 \end{Bmatrix}^T \begin{Bmatrix} \mathbf{Lu},_1 \\ \mathbf{Lu},_2 \\ \mathbf{Lu},_3 \end{Bmatrix}]d\Omega - \delta P^e . \tag{25}$$

By invoking the divergence theorem, its variation is

$$\delta\Pi^e = \int_{\Omega^e} [\begin{Bmatrix} \delta\widehat{\mathbf{m}}^1 \\ \delta\widehat{\mathbf{m}}^2 \\ \delta\widehat{\mathbf{m}}^3 \end{Bmatrix}^T (\begin{Bmatrix} \mathbf{Lu},_1 \\ \mathbf{Lu},_2 \\ \mathbf{Lu},_3 \end{Bmatrix} - \mathbf{C}_g^{-1}\begin{Bmatrix} \widehat{\mathbf{m}}^1 \\ \widehat{\mathbf{m}}^2 \\ \widehat{\mathbf{m}}^3 \end{Bmatrix}) - \delta\mathbf{u}^T \left(\mathbf{L}^T (\boldsymbol{\sigma} - \widehat{\mathbf{m}}^1,_1 -\widehat{\mathbf{m}}^2,_2 -\widehat{\mathbf{m}}^3,_3)\right)]d\Omega$$

$$+ \int_{\partial\Omega^e} ([\upsilon(n)(\boldsymbol{\sigma} - \widehat{\mathbf{m}}^1,_1 -\widehat{\mathbf{m}}^2,_2 -\widehat{\mathbf{m}}^3,_3)]^T \delta\mathbf{u} + (n_1\widehat{\mathbf{m}}^1 + n_2\widehat{\mathbf{m}}^2 + n_3\widehat{\mathbf{m}}^2)^T (\mathbf{L}\delta\mathbf{u}))dS - \delta P^e \tag{26}$$

On the element face, local Cartesian coordinates n, s and t are defined with unit vectors $\mathbf{e}_n = \{n_i\}$, $\mathbf{e}_s = \{s_i\}$ and $\mathbf{e}_t = \{t_i\}$, respectively, where $\mathbf{e}_n$ is pointing along the outward normal direction whilst $\mathbf{e}_s$ and $\mathbf{e}_t$ are two arbitrary tangential directions, see Figure 2(b). Similar to (13), one gets the following relations on the displacement-gradients defined with respect to (x_1, x_2, x_3) and (n,s,t)

$$\begin{Bmatrix} \mathbf{u},_n \\ \mathbf{u},_s \\ \mathbf{u},_t \end{Bmatrix} = \begin{bmatrix} n_1\mathbf{I}_3 & n_2\mathbf{I}_3 & n_3\mathbf{I}_3 \\ s_1\mathbf{I}_3 & s_2\mathbf{I}_3 & s_3\mathbf{I}_3 \\ t_1\mathbf{I}_3 & t_2\mathbf{I}_3 & t_3\mathbf{I}_3 \end{bmatrix}\begin{Bmatrix} \mathbf{u},_1 \\ \mathbf{u},_2 \\ \mathbf{u},_3 \end{Bmatrix} \quad \text{and} \quad \begin{Bmatrix} \mathbf{u},_1 \\ \mathbf{u},_2 \\ \mathbf{u},_3 \end{Bmatrix} = \begin{bmatrix} n_1\mathbf{I}_3 & n_2\mathbf{I}_3 & n_3\mathbf{I}_3 \\ s_1\mathbf{I}_3 & s_2\mathbf{I}_3 & s_3\mathbf{I}_3 \\ t_1\mathbf{I}_3 & t_2\mathbf{I}_3 & t_3\mathbf{I}_3 \end{bmatrix}^T\begin{Bmatrix} \mathbf{u},_r \\ \mathbf{u},_s \\ \mathbf{u},_t \end{Bmatrix} \tag{27a,b}$$

(27b) allows the second boundary integrand in (26) to be expressed in terms of the derivatives of $\mathbf{u}$ with respect to (n,s,t), and (26) can be re-written as

$$\delta\Pi^e = \int_{\Omega^e} [\begin{Bmatrix} \delta\widehat{\mathbf{m}}^1 \\ \delta\widehat{\mathbf{m}}^2 \\ \delta\widehat{\mathbf{m}}^3 \end{Bmatrix}^T (\begin{Bmatrix} \mathbf{Lu},_1 \\ \mathbf{Lu},_2 \\ \mathbf{Lu},_3 \end{Bmatrix} - \mathbf{C}_g^{-1}\begin{Bmatrix} \widehat{\mathbf{m}}^1 \\ \widehat{\mathbf{m}}^2 \\ \widehat{\mathbf{m}}^3 \end{Bmatrix}) - \delta\mathbf{u}^T \left(\mathbf{L}^T (\boldsymbol{\sigma} - \widehat{\mathbf{m}}^1,_1 -\widehat{\mathbf{m}}^2,_2 -\widehat{\mathbf{m}}^3,_3)\right)]d\Omega$$

$$+ \int_{\partial\Omega^e} [\mathbf{v}(n)(\boldsymbol{\sigma} - \hat{\mathbf{m}}^1,_1 - \hat{\mathbf{m}}^2,_2 - \hat{\mathbf{m}}^3,_3)]^T \delta\mathbf{u} + (\mathbf{v}_n \begin{Bmatrix} \hat{\mathbf{m}}^1 \\ \hat{\mathbf{m}}^2 \\ \hat{\mathbf{m}}^3 \end{Bmatrix})^T \delta\mathbf{u},_n + (\mathbf{v}_s \begin{Bmatrix} \hat{\mathbf{m}}^1 \\ \hat{\mathbf{m}}^2 \\ \hat{\mathbf{m}}^3 \end{Bmatrix})^T \delta\mathbf{u},_s + (\mathbf{v}_t \begin{Bmatrix} \hat{\mathbf{m}}^1 \\ \hat{\mathbf{m}}^2 \\ \hat{\mathbf{m}}^3 \end{Bmatrix})^T \delta\mathbf{u},_t] d\Gamma$$

$$- \delta P^e. \tag{28}$$

where

$$\mathbf{v}_n = [n_1\mathbf{v}(n), n_2\mathbf{v}(n), n_3\mathbf{v}(n)], \quad \mathbf{v}_s = [n_1\mathbf{v}(s), n_2\mathbf{v}(s), n_3\mathbf{v}(s)], \quad \mathbf{v}_t = [n_1\mathbf{v}(t), n_2\mathbf{v}(t), n_3\mathbf{v}(t)]$$

and $\mathbf{v}(\circ)$ has been defined under (3). If $\mathbf{u}$ is C^0, its tangential derivatives $\mathbf{u},_s$ and $\mathbf{u},_t$ would also be C^0. The only concern would be the compatibility of the normal derivative $\mathbf{u},_n$. Thus, by comparing with (21), the gradient elasticity counterpart of (24) could be written as:

$$\Pi_{RH}^e = \int_{\Omega^e} (\frac{1}{2}(\mathbf{Lu})^T \mathbf{C}_\varepsilon (\mathbf{Lu}) - \frac{1}{2} \begin{Bmatrix} \hat{\mathbf{m}}^1 \\ \hat{\mathbf{m}}^2 \\ \hat{\mathbf{m}}^3 \end{Bmatrix}^T \mathbf{C}_g^{-1} \begin{Bmatrix} \hat{\mathbf{m}}^1 \\ \hat{\mathbf{m}}^2 \\ \hat{\mathbf{m}}^3 \end{Bmatrix} + \begin{Bmatrix} \hat{\mathbf{m}}^1 \\ \hat{\mathbf{m}}^2 \\ \hat{\mathbf{m}}^3 \end{Bmatrix}^T \begin{Bmatrix} \mathbf{Lu},_1 \\ \mathbf{Lu},_2 \\ \mathbf{Lu},_3 \end{Bmatrix}] d\Omega - \int_{\partial\Omega^e} (\mathbf{v}_n \begin{Bmatrix} \hat{\mathbf{m}}_c^1 \\ \hat{\mathbf{m}}_c^2 \\ \hat{\mathbf{m}}_c^3 \end{Bmatrix})^T (\mathbf{u},_n - \tilde{\mathbf{u}}_n) dS$$

$$- P^e \tag{29}$$

in which $\tilde{\mathbf{u}}_n$ is an assumed compatible displacement-derivative along n; $\hat{\mathbf{m}}^1$, $\hat{\mathbf{m}}^2$ and $\hat{\mathbf{m}}^3$ are the assumed double stresses whilst $\hat{\mathbf{m}}_c^1$, $\hat{\mathbf{m}}_c^2$ and $\hat{\mathbf{m}}_c^3$ represent their constant modes, respectively. A Hu-Washizu functional similar to the above Π_{RH}^e was employed to justify the refined direct stiffness method (RDSM) for thin plate elements [36] whose element stiffness matrices can be computed simply by augmenting a refinement term to the B-matrix which relates the curvature and the element vector of dofs. However, the C^0 feature of deflection is not fully invoked in RDSM and a more succinct justification using the two-field functional in (29) will be presented in the next subsection for 3D gradient-elasticity. A 2D counterpart of the functional in (29) has been employed to formulate triangular and quadrilateral elements for plane gradient-elasticity by the corresponding author and his coworker [27].

5.3 Element Formulation

A compatible $\tilde{\mathbf{u}}_n$ can be obtained by linear interpolation of $\mathbf{u}_n$ which can be obtained via (27a) at the three nodes on each element face. The scheme can be symbolically expressed as

$$\tilde{\mathbf{u}}_n = \tilde{\mathbf{N}}_n \mathbf{d}. \tag{30}$$

Without loss of generality, the C^0 displacement in (12) can be expressed as

$$\mathbf{u}=\mathbf{Nd}=\mathbf{N}_o\boldsymbol{\alpha}_o+\mathbf{N}_c\boldsymbol{\alpha}_c+\mathbf{N}_n\boldsymbol{\alpha}_n \tag{31}$$

in which

$$\begin{bmatrix} (\mathbf{LN}_o),_1 \\ (\mathbf{LN}_o),_2 \\ (\mathbf{LN}_o),_3 \end{bmatrix}=\mathbf{0}_{18\times12} \ , \ \begin{bmatrix} (\mathbf{LN}_c),_1 \\ (\mathbf{LN}_c),_2 \\ (\mathbf{LN}_c),_3 \end{bmatrix}=\mathbf{I}_{18\times18} \ , \ \int_{\Omega^e}\begin{bmatrix} (\mathbf{LN}_n),_1 \\ (\mathbf{LN}_n),_2 \\ (\mathbf{LN}_n),_3 \end{bmatrix}d\Omega=\mathbf{0}_{18\times18}$$

and $\boldsymbol{\alpha}$s are linear combinations of the 48 dofs in the element vector of dofs $\mathbf{d}$. Here, $\boldsymbol{\alpha}_o$ embraces the 12 constant and linear displacement modes whilst $\boldsymbol{\alpha}_c$ embraces the 18 quadratic displacement modes in the basis of $\mathbf{u}$. The vanished nature of integrals of $(\mathbf{LN}_n),_i$ can always be attained via Schmidt-orthogonalization. Through deriving the strain-gradient and taking integration, (31) gives

$$\boldsymbol{\alpha}_c+\mathbf{B}_{gn}\boldsymbol{\alpha}_n=\mathbf{B}_g\mathbf{d} \quad\text{and}\quad \boldsymbol{\alpha}_c=\frac{1}{\Omega^e}\int_{\Omega^e}\mathbf{B}_g d\Omega\cdot\mathbf{d} \tag{32}$$

where

$$\mathbf{B}_{gn}=\begin{bmatrix} (\mathbf{LN}_n),_1 \\ (\mathbf{LN}_n),_2 \\ (\mathbf{LN}_n),_3 \end{bmatrix} , \ \mathbf{B}_g=\begin{bmatrix} (\mathbf{LN}),_1 \\ (\mathbf{LN}),_2 \\ (\mathbf{LN}),_3 \end{bmatrix} , \ \int_{\Omega^e}\mathbf{B}_{gn}d\Omega=\mathbf{0} \ \text{and}\ \Omega^e=\int_{\Omega^e}d\Omega.$$

For the assumed double-stresses, one can take

$$\begin{Bmatrix} \hat{\mathbf{m}}_c^1 \\ \hat{\mathbf{m}}_c^2 \\ \hat{\mathbf{m}}_c^3 \end{Bmatrix}=\mathbf{C}_g\boldsymbol{\beta}_c \quad\text{and}\quad \begin{Bmatrix} \hat{\mathbf{m}}^1 \\ \hat{\mathbf{m}}^2 \\ \hat{\mathbf{m}}^3 \end{Bmatrix}=\mathbf{C}_g[\mathbf{I}_{18},\mathbf{B}_{gn}]\begin{Bmatrix} \boldsymbol{\beta}_c \\ \boldsymbol{\beta}_n \end{Bmatrix} \tag{33a,b}$$

Substituting (30), (31) and (33) into (29), one gets

$$\Pi_{RH}^e=\frac{1}{2}\mathbf{d}^T\int_{\Omega^e}(\mathbf{LN})^T\mathbf{C}_\varepsilon(\mathbf{LN})d\Omega\cdot\mathbf{d}-\frac{1}{2}\begin{Bmatrix}\boldsymbol{\beta}_c\\\boldsymbol{\beta}_n\end{Bmatrix}^T\begin{bmatrix}\mathbf{H}_c & \mathbf{0}\\\mathbf{0} & \mathbf{H}_n\end{bmatrix}\begin{Bmatrix}\boldsymbol{\beta}_c\\\boldsymbol{\beta}_n\end{Bmatrix}+\begin{Bmatrix}\boldsymbol{\beta}_c\\\boldsymbol{\beta}_n\end{Bmatrix}^T\begin{bmatrix}\mathbf{G}_c\\\mathbf{G}_n\end{bmatrix}\mathbf{d}-P^e \tag{34}$$

where

$$\begin{bmatrix}\mathbf{H}_c\\\mathbf{H}_n\end{bmatrix}=\int_{\Omega^e}\begin{bmatrix}\mathbf{C}_g\\\mathbf{B}_{gn}^T\mathbf{C}_g\mathbf{B}_{gn}\end{bmatrix}d\Omega \ , \ \begin{bmatrix}\mathbf{G}_c\\\mathbf{G}_n\end{bmatrix}=\int_{\Omega^e}\begin{bmatrix}\mathbf{C}_g(\mathbf{B}_g-\mathbf{B}_{gR})\\\mathbf{B}_{gn}^T\mathbf{C}_g\mathbf{B}_g^T\end{bmatrix}d\Omega \ , \ \mathbf{B}_{gR}=\frac{1}{\Omega^e}\int_{\partial\Omega^e}\boldsymbol{\upsilon}_n^T(\mathbf{N},_n-\tilde{\mathbf{N}}_n)d\Gamma.$$

Variations of $\boldsymbol{\beta}_c$ and $\boldsymbol{\beta}_n$ in the functional enforce

$$\boldsymbol{\beta}_c=\mathbf{H}_c^{-1}\mathbf{G}_c\mathbf{d}=\frac{1}{\Omega^e}\int_{\Omega^e}(\mathbf{B}_g-\mathbf{B}_{gR})d\Omega\cdot\mathbf{d}=\boldsymbol{\alpha}_c-\mathbf{B}_{gR}\mathbf{d},$$

$$\boldsymbol{\beta}_n = \mathbf{H}_n^{-1}\mathbf{G}_n\mathbf{d} = (\int_{\Omega^e} \mathbf{B}_{gn}^T\mathbf{C}_g\mathbf{B}_{gn}^T d\Omega)^{-1} \int_{\Omega^e} \mathbf{B}_{gn}^T\mathbf{C}_g\mathbf{B}_g^T d\Omega \cdot \mathbf{d} = \boldsymbol{\alpha}_n \tag{35a,b}$$

and

$$[\mathbf{I}_{18}, \mathbf{B}_{gn}]\left\{\begin{array}{c}\boldsymbol{\beta}_c \\ \boldsymbol{\beta}_n\end{array}\right\} = [\mathbf{I}_{18}, \mathbf{B}_{gn}]\left\{\begin{array}{c}\boldsymbol{\alpha}_c - \mathbf{B}_{gR}\mathbf{d} \\ \boldsymbol{\alpha}_n\end{array}\right\} = (\mathbf{B}_g - \mathbf{B}_{gR})\mathbf{d} \ , \ \left\{\begin{array}{c}\widehat{\mathbf{m}}^1 \\ \widehat{\mathbf{m}}^2 \\ \widehat{\mathbf{m}}^3\end{array}\right\} = \mathbf{C}_g \ [\mathbf{I}_{18}, \mathbf{B}_{gn}]\left\{\begin{array}{c}\boldsymbol{\beta}_c \\ \boldsymbol{\beta}_n\end{array}\right\} = \mathbf{C}_g(\mathbf{B}_g - \mathbf{B}_{gR})\mathbf{d}$$

$$\tag{36a,b}$$

in which the relations in (32) have been invoked.

With $\mathbf{H}_c\boldsymbol{\beta}_c = \mathbf{G}_c\mathbf{d}$ and $\mathbf{H}_n\boldsymbol{\beta}_n = \mathbf{G}_n\mathbf{d}$ substituted into the relaxed-hybrid functional in (34), the latter becomes

$$\Pi_{RH}^e = \frac{1}{2}\mathbf{d}^T \int_{\Omega^e} (\mathbf{LN})^T\mathbf{C}_\varepsilon(\mathbf{LN})d\Omega \cdot \mathbf{d} + \frac{1}{2}\left\{\begin{array}{c}\boldsymbol{\beta}_c \\ \boldsymbol{\beta}_n\end{array}\right\}^T\left[\begin{array}{cc}\mathbf{H}_c & \mathbf{0} \\ \mathbf{0} & \mathbf{H}_n\end{array}\right]\left\{\begin{array}{c}\boldsymbol{\beta}_c \\ \boldsymbol{\beta}_n\end{array}\right\} - P^e \tag{37}$$

By invoking (36a),

$$\Pi_{RH}^e = \frac{1}{2}\mathbf{d}^T \int_{\Omega^e} [(\mathbf{LN})^T\mathbf{C}_\varepsilon(\mathbf{LN}) + (\mathbf{B}_g - \mathbf{B}_{gR})^T\mathbf{C}_g(\mathbf{B}_g - \mathbf{B}_{gR})]d\Omega \cdot \mathbf{d} - P^e = \frac{1}{2}\mathbf{d}^T\mathbf{k}_{RH}\mathbf{d} - P^e \tag{38}$$

where the element stiffness matrix $\mathbf{k}_{RH}$ for the relaxed-hybrid element RHT4 is self-defined. For the element, the strain-displacement matrix is $\mathbf{LN}$, which is the same as that of DKT4, and the strain-gradient-displacement matrix is $(\mathbf{B}_g - \mathbf{B}_{gR})$.

It can be noted that the element stiffness matrix assumed a format similar to those derived from RDSM [36, 37]. However, there are a few differences between the present approach and RDSM. Firstly, the present approach starts from a C^0 displacement which leads to the strain and strain-gradient. On the other hand, two largely independent sets of displacement are employed to derive the strain and strain-gradient in RDSM. Secondly, the refinement matrix analogous to $\mathbf{B}_{gR}$ in RDSM involves the correction with respect to discontinuous $\mathbf{u}_{,n}$, $\mathbf{u}_{,s}$ and $\mathbf{u}_{,t}$ but the present $\mathbf{B}_{gR}$ involves the refinement with respect to discontinuous $\mathbf{u}_{,n}$ only. Finally, the present proof is given for strain-gradient elasticity problem via a relaxed two-field Hellinger-Reissner functional instead of the simpler thin-plate problem via a more complicated relaxed three-field Hu-Washizu functional.

5.4 Generalized Individual Element Patch Test

To examine whether $\mathbf{k}_{RH}$ passes the individual element patch test, $\mathbf{u}_Q$ and the derived quantities

in (19) are considered. Since $\mathbf{N}$ can reproduce the quadratic $\mathbf{u}_Q$ and $\tilde{\mathbf{N}}_n$ can reproduce the linear $\mathbf{u}_{Q,n}$,

$(\mathbf{N}_{,n} - \tilde{\mathbf{N}}_n)\mathbf{d}_Q = \mathbf{0}$ and $\mathbf{B}_{gR}\mathbf{d}_Q = \mathbf{0}$. Thus,

$$\mathbf{k}_{RH}\mathbf{d}_Q = \int_{\Omega^e} [(\mathbf{LN})^T \boldsymbol{\sigma}_Q + \left(\begin{bmatrix} (\mathbf{LN})_{,1} \\ (\mathbf{LN})_{,2} \\ (\mathbf{LN})_{,3} \end{bmatrix} - \mathbf{B}_{gR} \right)^T \begin{Bmatrix} \mathbf{m}_Q^1 \\ \mathbf{m}_Q^2 \\ \mathbf{m}_Q^3 \end{Bmatrix}] d\Omega$$

$$= \int_{\partial\Omega^e} [\mathbf{N}^T \boldsymbol{\upsilon}\boldsymbol{\sigma}_Q + (\mathbf{LN})^T (n_1 \mathbf{m}_Q^1 + n_2 \mathbf{m}_Q^2 + n_3 \mathbf{m}_Q^3) - (\mathbf{N}_{,n} - \tilde{\mathbf{N}}_n)^T \boldsymbol{\upsilon}_n \begin{Bmatrix} \mathbf{m}_Q^1 \\ \mathbf{m}_Q^2 \\ \mathbf{m}_Q^3 \end{Bmatrix}] d\Gamma . \qquad (39)$$

Same as the first proposed element, one must use at least the 5-point and 4-point integration rules for the domain integrals involving $\boldsymbol{\sigma}_Q$ and $(\mathbf{m}_Q^1, \mathbf{m}_Q^2, \mathbf{m}_Q^3)$, respectively. By invoking

$$n_1(\mathbf{LN})^T \mathbf{m}_Q^1 + n_2(\mathbf{LN})^T \mathbf{m}_Q^2 + n_3(\mathbf{LN})^T \mathbf{m}_Q^3 = \mathbf{N}_{,n}^T \boldsymbol{\upsilon}_n \begin{Bmatrix} \mathbf{m}_Q^1 \\ \mathbf{m}_Q^2 \\ \mathbf{m}_Q^3 \end{Bmatrix} + \mathbf{N}_{,s}^T \boldsymbol{\upsilon}_s \begin{Bmatrix} \mathbf{m}_Q^1 \\ \mathbf{m}_Q^2 \\ \mathbf{m}_Q^3 \end{Bmatrix} + \mathbf{N}_{,t}^T \boldsymbol{\upsilon}_t \begin{Bmatrix} \mathbf{m}_Q^1 \\ \mathbf{m}_Q^2 \\ \mathbf{m}_Q^3 \end{Bmatrix}, \qquad (40)$$

(39) becomes

$$\mathbf{k}_{RH}\mathbf{d}_Q = \int_{\partial\Omega^e} [\mathbf{N}^T \boldsymbol{\upsilon}(n)\boldsymbol{\sigma}_Q + \mathbf{N}_{,s}^T \boldsymbol{\upsilon}_s \begin{Bmatrix} \mathbf{m}_Q^1 \\ \mathbf{m}_Q^2 \\ \mathbf{m}_Q^3 \end{Bmatrix} + \tilde{\mathbf{N}}_n^T \boldsymbol{\upsilon}_n \begin{Bmatrix} \mathbf{m}_Q^1 \\ \mathbf{m}_Q^2 \\ \mathbf{m}_Q^3 \end{Bmatrix} + \mathbf{N}_{,t}^T \boldsymbol{\upsilon}_t \begin{Bmatrix} \mathbf{m}_Q^1 \\ \mathbf{m}_Q^2 \\ \mathbf{m}_Q^3 \end{Bmatrix}] d\Gamma . \qquad (41)$$

As $\mathbf{N}$ is compatible, $\mathbf{N}_{,s}$ and $\mathbf{N}_{,t}$ are also compatible. $\tilde{\mathbf{N}}_n$ obtained by linearly interpolating $\mathbf{u}_{,n}$ at the nodes bounding each element edge is also compatible. Hence, pairwise cancellation of the generalized boundary forces occurs when (20) is assembled. As far as the employed integration rule for evaluating $\mathbf{k}_{RH}$ satisfies the orders identified under (39) and leads to a rank sufficient $\mathbf{k}_{RH}$, the element passes IET and, thus, the generalized patch test.

6. Numerical Benchmark Tests

In this section, numerical examples are employed to test the accuracy of the two proposed 4-node 48-dofs tetrahedral element models for strain-gradient analysis, namely

- DKT4: the generalized Discrete Kirchhoff element presented in Section 4,
- RHT4: the relaxed-hybrid element presented in Section 5.

Although the 4-point integration rule can be used to evaluate the element stiffness matrices associated with the strain-gradient/double-stress in the two elements without jeopardizing the constant double-stress patch test, they are evaluated by the 5-point integration rule for convenience. It has also been checked that the element predictions remain practically intact when the 4-point integration rule is employed to evaluate the matrices associated with the strain gradient/double-stress in these two elements, respectively. In all examples, the material is assumed to be isotropic. The material matrices are

$$
\mathbf{C}_\varepsilon = \begin{bmatrix}
2\mu+\lambda & \lambda & \lambda & 0 & 0 & 0 \\
\lambda & 2\mu+\lambda & \lambda & 0 & 0 & 0 \\
\lambda & \lambda & 2\mu+\lambda & 0 & 0 & 0 \\
0 & 0 & 0 & \mu & 0 & 0 \\
0 & 0 & 0 & 0 & \mu & 0 \\
0 & 0 & 0 & 0 & 0 & \mu
\end{bmatrix}
\quad \text{and} \quad
\mathbf{C}_g = l^2 \begin{bmatrix}
\mathbf{C}_\varepsilon & \mathbf{0}_{6\times6} & \mathbf{0}_{6\times6} \\
\mathbf{0}_{6\times6} & \mathbf{C}_\varepsilon & \mathbf{0}_{6\times6} \\
\mathbf{0}_{6\times6} & \mathbf{0}_{6\times6} & \mathbf{C}_\varepsilon
\end{bmatrix}
\qquad (42a,b)
$$

where

$$
\mu = \frac{E}{2(1+\nu)} \;,\quad \lambda = \frac{\nu E}{(1+\nu)(1-2\nu)} \;,
$$

E is the elastic modulus, ν is the Poisson's ratio and l is the intrinsic length accounting for the material size effect. The material constants are taken, rather arbitrarily, to be $\mu = 1$, $\lambda = 2$ and $l = 0.3$ or 0.003. The meshes are generated by ABAQUS and the formulations are implemented by using ABAQUS user-defined element subroutine UEL. The following relative stress error norm E_s, relative double-stress error norm E_m and the relative energy error norm E_w are defined to evaluate the element accuracy and convergence:

$$
E_s = \sqrt{\frac{\displaystyle\sum_e \int_{\Omega^e} (\boldsymbol{\sigma}-\boldsymbol{\sigma}_{exact})^T \mathbf{C}_\varepsilon^{-1}(\boldsymbol{\sigma}-\boldsymbol{\sigma}_{exact})\, d\Omega}{\displaystyle\sum_e \int_{\Omega^e} \boldsymbol{\sigma}_{exact}^T \mathbf{C}_\varepsilon^{-1}\boldsymbol{\sigma}_{exact}\, d\Omega}}
$$

$$
E_m = \sqrt{\frac{\displaystyle\sum_e \int_{\Omega^e} \left(\left\{\begin{matrix}\mathbf{m}^1\\\mathbf{m}^2\\\mathbf{m}^3\end{matrix}\right\}-\left\{\begin{matrix}\mathbf{m}^1_{exact}\\\mathbf{m}^2_{exact}\\\mathbf{m}^3_{exact}\end{matrix}\right\}\right)^T \mathbf{C}_g^{-1}\left(\left\{\begin{matrix}\mathbf{m}^1\\\mathbf{m}^2\\\mathbf{m}^3\end{matrix}\right\}-\left\{\begin{matrix}\mathbf{m}^1_{exact}\\\mathbf{m}^2_{exact}\\\mathbf{m}^3_{exact}\end{matrix}\right\}\right)d\Omega}{\displaystyle\sum_e \int_{\Omega^e} \left\{\begin{matrix}\mathbf{m}^1_{exact}\\\mathbf{m}^2_{exact}\\\mathbf{m}^3_{exact}\end{matrix}\right\}^T \mathbf{C}_g^{-1}\left\{\begin{matrix}\mathbf{m}^1_{exact}\\\mathbf{m}^2_{exact}\\\mathbf{m}^3_{exact}\end{matrix}\right\}d\Omega}} \;,
$$

$$E_w = \sqrt{\dfrac{\displaystyle\sum_e \int_{\Omega^e} [(\boldsymbol{\sigma}-\boldsymbol{\sigma}_{exact})^T \mathbf{C}_\varepsilon^{-1}(\boldsymbol{\sigma}-\boldsymbol{\sigma}_{exact}) + (\left\{\begin{matrix}\mathbf{m}^1\\\mathbf{m}^2\\\mathbf{m}^3\end{matrix}\right\} - \left\{\begin{matrix}\mathbf{m}^1_{exact}\\\mathbf{m}^2_{exact}\\\mathbf{m}^3_{exact}\end{matrix}\right\})^T \mathbf{C}_g^{-1}(\left\{\begin{matrix}\mathbf{m}^1\\\mathbf{m}^2\\\mathbf{m}^3\end{matrix}\right\} - \left\{\begin{matrix}\mathbf{m}^1_{exact}\\\mathbf{m}^2_{exact}\\\mathbf{m}^3_{exact}\end{matrix}\right\})]\,d\Omega}{\displaystyle\sum_e \int_{\Omega^e} (\boldsymbol{\sigma}_{exact}^T \mathbf{C}_\varepsilon^{-1}\boldsymbol{\sigma}_{exact} + \left\{\begin{matrix}\mathbf{m}^1_{exact}\\\mathbf{m}^2_{exact}\\\mathbf{m}^3_{exact}\end{matrix}\right\}^T \mathbf{C}_g^{-1}\left\{\begin{matrix}\mathbf{m}^1_{exact}\\\mathbf{m}^2_{exact}\\\mathbf{m}^3_{exact}\end{matrix}\right\}]\,d\Omega}} \qquad .(43\text{a,b,c})$$

The following ratio R for the strain energies associate with the strain and strain-gradient is also computed:

$$R = \dfrac{\displaystyle\sum_e \int_{\Omega^e} \boldsymbol{\sigma}_{exact}^T \mathbf{C}_\varepsilon^{-1}\boldsymbol{\sigma}_{exact}^T\,d\Omega}{\displaystyle\sum_e \int_{\Omega^e} \left\{\begin{matrix}\mathbf{m}^1_{exact}\\\mathbf{m}^2_{exact}\\\mathbf{m}^3_{exact}\end{matrix}\right\}^T \mathbf{C}_g^{-1}\left\{\begin{matrix}\mathbf{m}^1_{exact}\\\mathbf{m}^2_{exact}\\\mathbf{m}^3_{exact}\end{matrix}\right\}\,d\Omega} \qquad (44)$$

All terms defined in (43) and (44) are evaluated by the 5-point integration rule. A large R implies that the strain/stress dominates in the minimization of the potential energy functional. Thus, the strain-gradient/double-stress would be more erroneous.

The error for a field variable in the finite element analysis is well-known to be ~O(hp+1-m) in which h is the element size, p is the element interpolation order, and m is the derivative order of the field variable. The present elements are complete quadrature but incomplete cubic in interpolation order, that is, p = 2, whereas m= 1 for stress and m = 2 for the double-stress. For 3D analyses, h $\propto$ (nDOF)−1/3 where nDOF is the number of nodal dofs. Thus,

$$E_s \sim O\left((nDOF)^{-2/3}\right), \quad E_m \sim O\left((nDOF)^{-1/3}\right) \qquad (45\text{a,b})$$

In the log-log plots for E_s and E_m against nDOF, the magnitudes of the slope are expected to be 2/3 and 1/3, respectively.

6.1 Constant Double-Stress Patch Test

In this test, 1×1×1 cuboid in Figure 3 is considered. It is meshed into 35 elements with internal nodes and elements away from the boundary of the cuboid. The following displacement is employed for the constant double-stress patch test

$$\left\{\begin{matrix}u_1\\u_2\\u_3\end{matrix}\right\} = \frac{1}{100}\left\{\begin{matrix}4x_1+4x_2+4x_3+4x_1^2-41x_2^2+4x_3^2+4x_1x_2+4x_1x_3+4x_2x_3\\48x_1+6x_2+6x_3-48x_1^2+6x_2^2+6x_3^2+6x_1x_2+6x_1x_3+6x_2x_3\\-8x_1+55x_2+8x_3+8x_1^2-55x_2^2+8x_3^2+8x_1x_2+8x_1x_3+8x_2x_3\end{matrix}\right\} \qquad (46)$$

which leads to the equilibrating stress and double-stress below

$$\boldsymbol{\sigma} = \left\{\begin{matrix} \sigma_{11} \\ \sigma_{22} \\ \sigma_{33} \\ \sigma_{13} \\ \sigma_{12} \\ \sigma_{23} \end{matrix}\right\} = \frac{1}{100}\left\{\begin{matrix} 44 \\ 48 \\ 52 \\ -4 \\ 52 \\ 61 \end{matrix}\right\} + \frac{x_1}{100}\left\{\begin{matrix} 60 \\ 56 \\ 60 \\ 20 \\ -92 \\ 14 \end{matrix}\right\} + \frac{x_2}{100}\left\{\begin{matrix} 56 \\ 72 \\ 64 \\ 12 \\ -76 \\ -104 \end{matrix}\right\} + \frac{x_3}{100}\left\{\begin{matrix} 60 \\ 64 \\ 84 \\ 16 \\ 10 \\ 20 \end{matrix}\right\},$$

$$\mathbf{m}^1 = \left\{\begin{matrix} m_{111} \\ m_{122} \\ m_{133} \\ m_{113} \\ m_{112} \\ m_{123} \end{matrix}\right\} = \frac{l^2}{100}\left\{\begin{matrix} 60 \\ 56 \\ 60 \\ 20 \\ -92 \\ 14 \end{matrix}\right\}, \quad \mathbf{m}^2 = \left\{\begin{matrix} m_{211} \\ m_{222} \\ m_{233} \\ m_{213} \\ m_{212} \\ m_{223} \end{matrix}\right\} = \frac{l^2}{100}\left\{\begin{matrix} 56 \\ 72 \\ 64 \\ 12 \\ -76 \\ -104 \end{matrix}\right\}, \quad \mathbf{m}^3 = \left\{\begin{matrix} m_{311} \\ m_{322} \\ m_{333} \\ m_{313} \\ m_{312} \\ m_{323} \end{matrix}\right\} = \frac{l^2}{100}\left\{\begin{matrix} 60 \\ 64 \\ 84 \\ 16 \\ 10 \\ 20 \end{matrix}\right\}. \quad (47\text{a-d})$$

To prevent the rigid body motion, $u_1 = u_2 = u_3 = 0$ is prescribed at node O, $u_2 = u_3 = 0$ is imposed at node B and $u_3 = 0$ is prescribed at node C. At the remaining dofs of the boundary nodes, natural boundary conditions are prescribed according to analytical solution. Both DKT4 and RHT4 pass the patch test by reproducing the displacement, stress and double-stress solutions exactly.
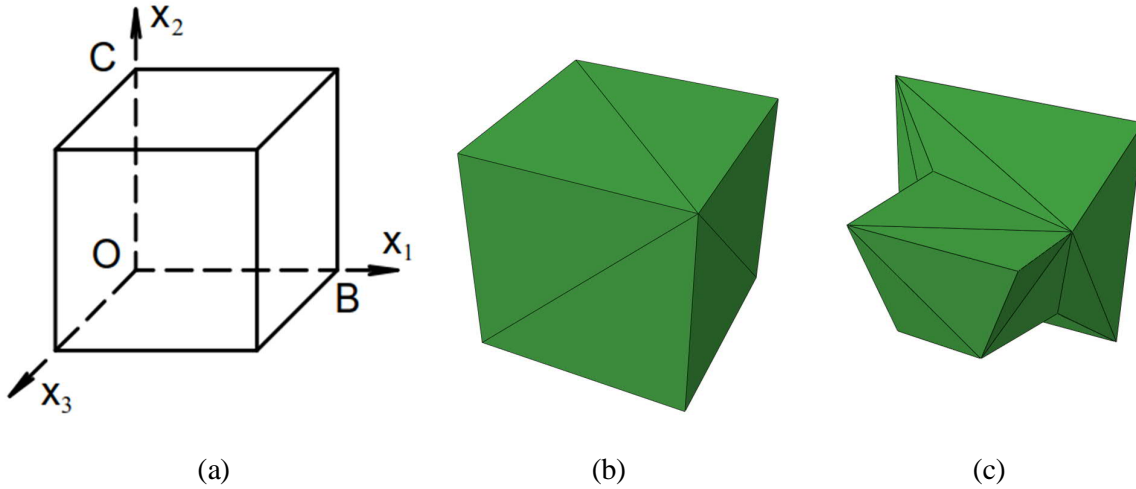

(a) (b) (c)

Figure 3. (a) The 1×1×1 cuboid employed for contant double-stress patch test. (b) The mesh modelling the cuboid. (c) The mesh with some elements removed.

6.2 Third-Order and Fourth-Order Tests

In these two examples, meshes with 36, 238, 1432 and 8481 elements, see Figure 4, are employed to model the 4×4×1 rectangular prism in Figure 4. In this example, essential boundary conditions are prescribed according to the following third-order and fourth-order displacement fields

$$\begin{Bmatrix} u_1 \\ u_2 \\ u_3 \end{Bmatrix} = \frac{1}{30000} \begin{Bmatrix} -948x_1 + 15x_2 + 33x_1^2 + 82x_1 x_2 - 195x_2^2 + 51x_1^3 - 150x_1^2 x_2 - 882x_1 x_2^2 + 128x_2^3 \\ 12x_1 + 18x_2 - 219x_1^2 + 42x_1 x_2 + 24x_2^2 + 54x_1^3 + 90x_1^2 x_2 + 72x_1 x_2^2 + 213x_2^3 \\ 0 \end{Bmatrix},$$

$$\begin{Bmatrix} u_1 \\ u_2 \\ u_3 \end{Bmatrix} = \frac{1}{90000} \begin{Bmatrix} -20700x_1 + 45x_2 + 99x_1^2 + 3318x_1 x_2 - 585x_2^2 + 153x_1^3 - 450x_1^2 x_2 - 2646x_1 x_2^2 + 384x_2^3 \\ 36x_1 + 54x_2 - 5265x_1^2 + 126x_1 x_2 + 72x_2^2 + 162x_1^3 + 270x_1^2 x_2 + 216x_1 x_2^2 + 639x_2^3 \\ 0 \end{Bmatrix}$$

$$\begin{matrix} +279x_1^4 - 736x_1^3 x_2^1 - 135x_1^2 x_2^2 + 2152x_1 x_2^3 - 234x_2^4 \\ +288x_1^4 - 1458x_1^3 x_2^1 + 396x_1^2 x_2^2 + 432x_1 x_2^3 - 420x_2^4 \end{matrix} \Bigg\} . \tag{48a,b}$$

Both of them lead to equilibrating stress and double-stress fields.

In the third-order test, $R \sim 29.0$ and 290 000 for $l = 0.3$ and 0.003, respectively. In the fourth-order test, $R \sim 6.78$ and 67 800 for $l = 0.3$ and 0.003, respectively. For the two tests, E_s and E_m are plotted against nDOF in Figures 5 and 6. Both models yield similar results and, as expected, they are more accurate in the third-order than the fourth-order test. E_s is markedly smaller than E_m probably because the strain is a lower order derivative of the displacement than the strain-gradient and R is large. In the case of $l = 0.003$, the two element models yield nearly identical results. The observation is sensible in the view that both elements use the same strain-displacement matrix **LN** and R is over 60 000 in both tests. Using the data from the coarse stand finest meshes, the slopes for E_s and E_m in Figure 5 are ~ 0.79 and ~ 0.42, respectively, whilst those in Figure 6 are ~ 0.77 and ~ 0.41, respectively. The convergence rates for E_s and E_m are higher than the estimations 2/3 and 1/3, respectively, in (45). E_w is not plotted. For $l = 0.3$ in the third-order (fourth-order) test, E_w/E_s increases from ~ 1.2 (~ 1.1) in coarsest mesh to ~ 3.4 (~ 3.3) in the finest mesh. Thus, theconvergent rate of E_w isslightly lower than that of E_s. For $l = 0.003$, E_w is practically identical to E_s due to the large R.
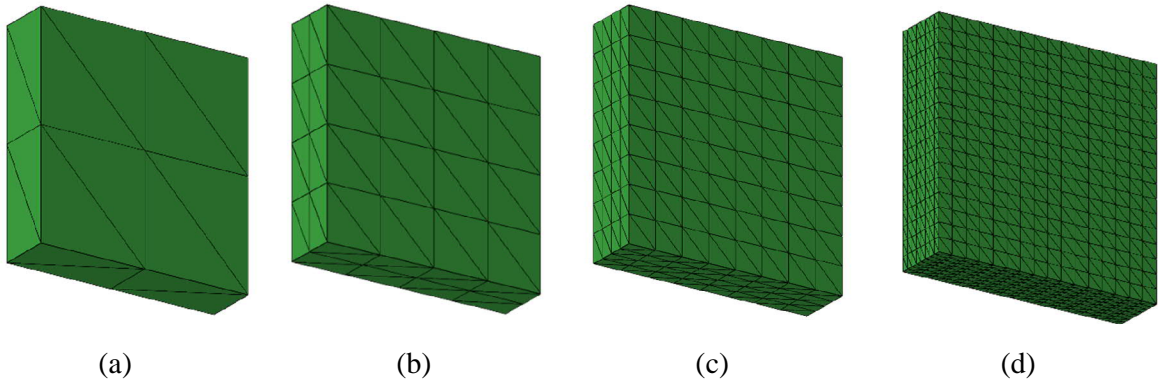

| (a) | (b) | (c) | (d) |

Figure 4. A 4×4×1 rectangular prism is meshed into (a) 36, (b) 238, (c) 1432 and (d) 8481 elements.
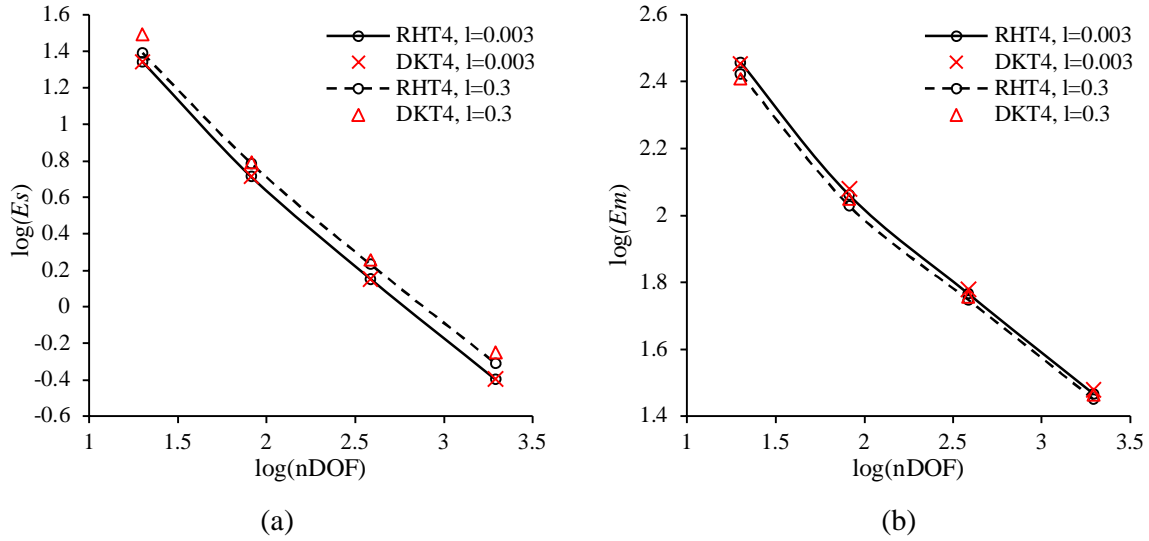
(a)   (b)

Figure 5. (a) E_s and (b) E_m against nDOF for the third-order test, see (48a) and Figure 4.
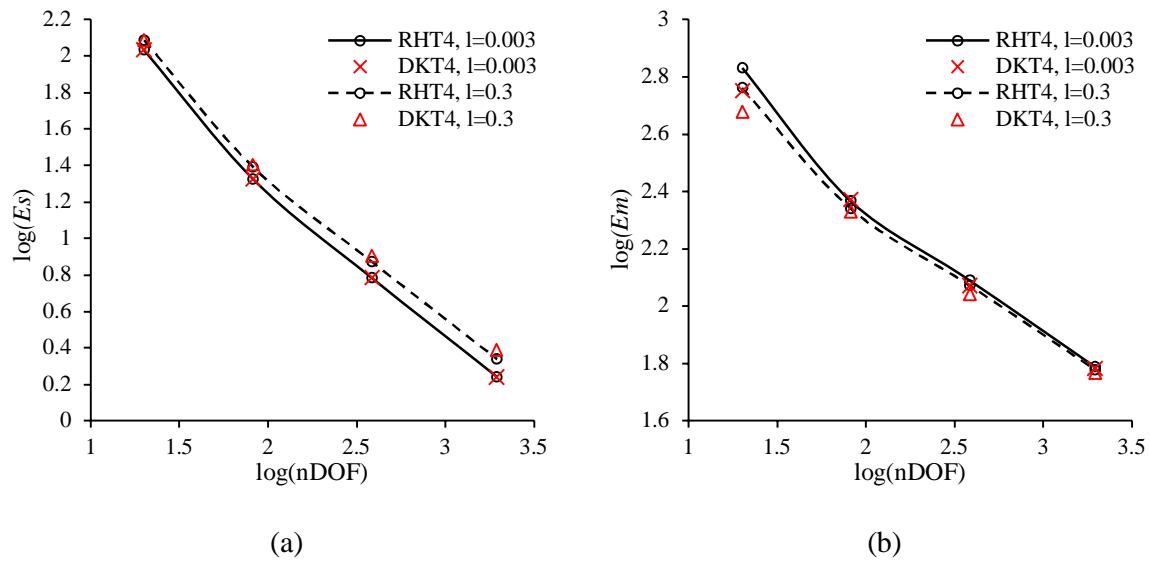

(a)   (b)

Figure 6. (a) E_s and (B) E_m against nDOF for the fourth-order test, see (48b) and Figure 4.

6.3 Flat Panel with a Cylindrical Cutout

This example considers a unit thickness 8×8 square panel with a central cylindrical cutout. Owing to symmetry, only one quarter of the problem is modelled and the 4×4×1 computational domain is meshed into 176, 1097, 7789 and 50446 elements, see Figure 5. On the boundary planes D and C, traction and double-traction derived from the following axial symmetric displacement field are prescribed [38]:

$$\begin{Bmatrix} u_1 \\ u_2 \end{Bmatrix} = \frac{p}{2\mu r f_3}[f_1 - al(1-2\nu)f_2]\begin{Bmatrix} \cos\theta \\ \sin\theta \end{Bmatrix}, \quad u_3 = 0 \tag{49}$$

where

$$f_1 = (\nu-1)a^4 + (2\nu-1)[2l^2 - r^2(\nu-1)]a^2 - 4(\nu-1)r^2l^2(2\nu-1)\,K_1(a/l),$$

$$f_2 = [a^2 - r^2(\nu-1)]\,K_0(a/l) - 2lr\,K_1(r/l), \quad f_3 = (a^2 + 4l^2)(\nu-1)K_1(a/l) + 2al(\nu-1/2)K_0(a/l),$$

(r, θ, x_3) are cylindrical coordinates, $a = 1$ is the radius of the cutout, p is radial stress at $r = \infty$,

K_n is the n-th order modified Bessel functions of the second kind.

Symmetric conditions are prescribed on the planes of symmetry B and E whilst traction-free and double-traction-free conditions are prescribed on the remaining boundary.
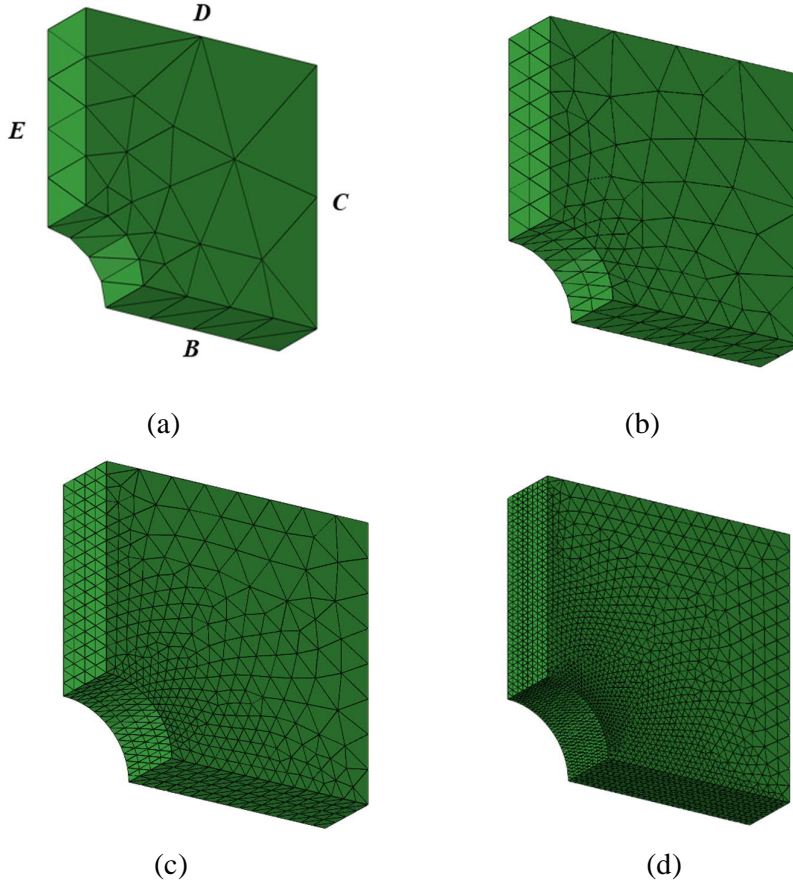

(a)   (b)

(c)   (d)

Figure 7. The 4×4×1 computational domain for a quarter of a square panel with a central circular cutout of unit radius is meshed into (a) 176, (b) 1097, (c) 7789 and (d) 50446 elements.

In this test, $R = 41$ and 206 000 for $l = 0.3$ and 0.003, respectively. E_s and E_m are plotted against nDOF in Figure 8. The two element models yield close E_s. On the other hand, RHT4 yields a slightly

smaller and larger E_m than DKT4 when l = 0.3 and 0.003, respectively. Using the data of the coarsest and finest meshes, the slopes of E_s and E_m are ~0.69 and ~0.32 which are again slightly higher than and close to the estimations 2/3 and 1/3, respectively, in (45). E_w is not plotted. For $l = 0.3$, E_w/E_s increases from ~1.4 in the coarsest mesh to ~6.3 in the finest mesh. Thus, the convergent rate of E_w is slightly lower than that of E_s. For $l = 0.003$, E_w is practically identical to E_s as R is large.
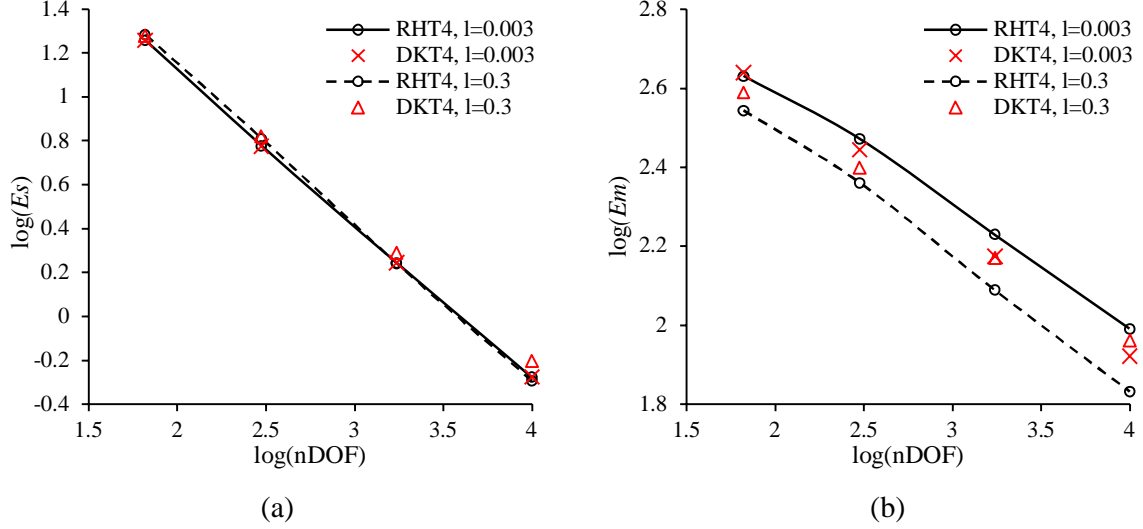

(a)   (b)

Figure 8. (a) E_s and (b) E_m against nDOF for the cylindrical cutout problem, see Figure 7.

6.4 Cube with a Spherical Void

This example considers an 8×8×8 cube with a central spherical void of unit radius. Owing to symmetry, only one-eighth of the problem is modelled and the 4×4×4 computational domain is meshed into 330, 2 091, 14 514 and 86 606 elements, see Figure 9. Over the 3 square boundary planes, traction and double-traction derived from the following displacement solution are prescribed [39]:

$$u_r = \frac{p}{8\left(3\lambda\mu+2\mu^2\right)\left(\mu f_1 + \lambda f_2\right)}\left[\mu(\frac{3}{2}\lambda+\mu)e^{\frac{a-r}{l}}f_3 - \mu^2 f_4 + 8\lambda\mu f_5 + 3\lambda^2 f_6\right], \quad u_\theta = u_\varphi = 0$$

(50a,b)

or, equivalently,

$$\begin{Bmatrix} u_1 \\ u_2 \\ u_3 \end{Bmatrix} = \frac{p}{8\left(3\lambda\mu+2\mu^2\right)\left(\mu f_1 + \lambda f_2\right)}\left[(\frac{3}{2}\lambda\mu+\mu^2)e^{\frac{a-r}{l}}f_3 - \mu^2 f_4 + 8\lambda\mu f_5 + 3\lambda^2 f_6\right]\begin{Bmatrix} \cos\theta\cos\varphi \\ \sin\theta\cos\varphi \\ \sin\varphi \end{Bmatrix}$$

(51)

where

$$f_1 = r^2 \left(a^3 + 3a^2l + 9al^2 + 9l^3\right), \quad f_2 = \frac{r^2}{2}\left(a^3 + a^2l + 9al^2 + 9l^3\right),$$

$$f_3 = -24l^2a^3\left(l+r\right), \quad f_4 = a^3(4a^3 + 12a^2l + 24a\ l^2 + 24l^3) + r^3\left(8a^3 + 24a^2l + 72al^2 + 72l^3\right),$$

$$f_5 = \frac{a^3}{2}(2a^3 + 5a^2l + 9a\ l^2 + 9l^3) + \frac{r^3}{2}(a^3 + a^2l + 9al^2 + 9l^3), f_6 = a^6 + a^5l,$$

(r,θ,φ) are spherical coordinates, $a = 1$ is the radius of the void, p is radial stress at $r = \infty$.

Symmetric conditions are prescribed over the three planes of symmetry whilst traction and double-traction free conditions are prescribed over the boundary of the spherical void.
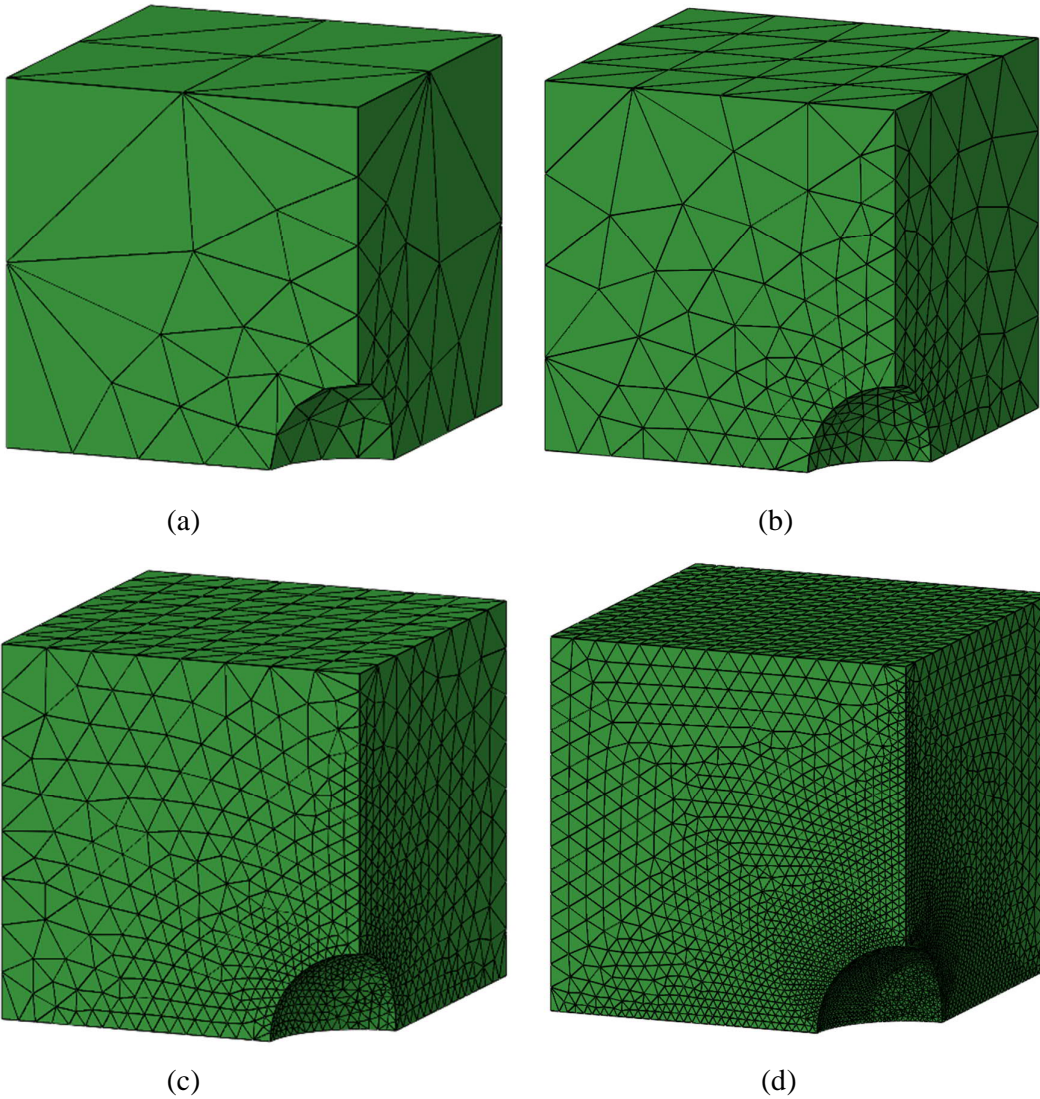

(a)

(b)

(c)

(d)

Figure 9. The 4×4×4 computational domain for one-eighth of a cube with a central spherical cutout of unit radius is meshed into (a) 1128, (b) 3969, (c) 4937 and (d) 86 606 elements.

In this test, $R = 270$ and $760\,000$ for $l = 0.3$ and 0.003, respectively. E_s and E_m are plotted against

nDOF in Figure 10. The two element models yield close E_s. On the other hand, RHT4 yields a slightly lower E_m than DKT4 when $l = 0.3$ but the two E_m are close when $l = 0.003$. Using the data of the coarsest and finest meshes, the slopes of E_s and E_m are ~0.73 and ~0.33 which are slightly higher than and close to the estimations 2/3 and 1/3, respectively, in (45). E_w is not plotted. For $l = 0.3$, E_w/E_s increases from ~1.2 in coarsest mesh to ~5.0 in the finest mesh. Thus, the convergent rate of E_w is slightly lower than that of the E_s. For $l = 0.003$, E_w is practically identical to E_s as R is large.

(a)   (b)
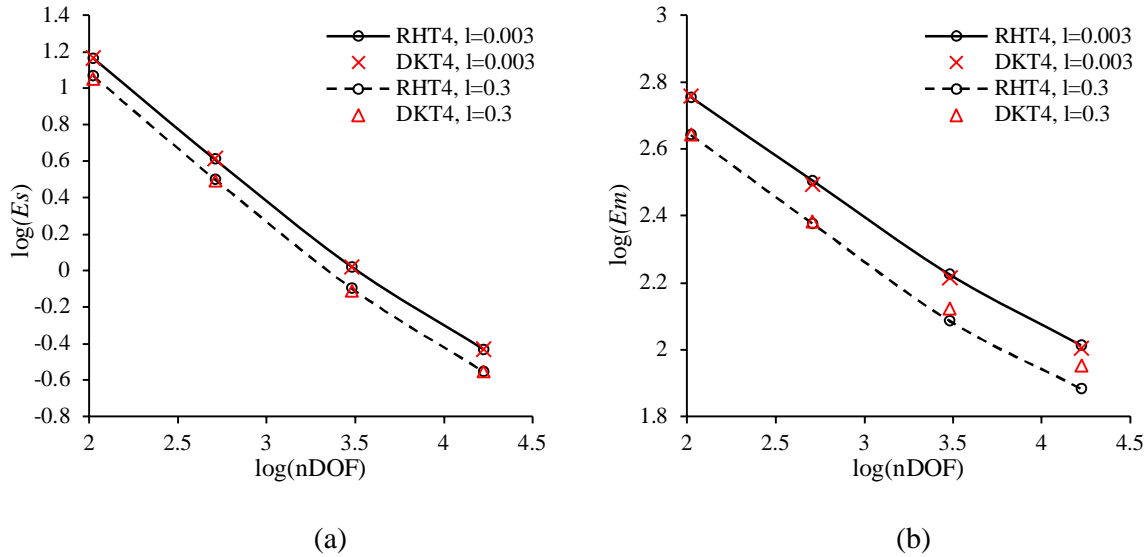
Figure 10. (a) E_s and (b) E_m against nDOF for the spherical void problem, see Figure 9.

8. Closure

In this paper, two 4-node 48-dof tetrahedral elements for strain-gradient elasticity analysis are devised based on the generalized discrete Kirchhoff and the relax-hybrid methods previously developed for formulating plane elements for gradient-elasticity analyses [27]. All nodes possess 12 dofs which include the displacement $\mathbf{u}$ and the displacement-gradient ($\mathbf{u}_{,1}$, $\mathbf{u}_{,2}$, $\mathbf{u}_{,3}$). To enable the elements to pass the constant double-stress patch test, a C^0 quadratic-complete displacement interpolation is first constructed. The strain in both elements are derived by taking derivative of the displacement interpolation. In the generalized discrete Kirchhoff element DKT4, the displacement-gradients at the mid-edge points are obtained from the nodal dofs. They together with those at the nodes are interpolated using the 10-node interpolation. The strain-gradient is then obtained by taking derivative of the interpolated displacement-gradient. In the relaxed-hybrid element RHT4, the strain-gradient is also derived from the displacement interpolation and the matrix relating the strain-gradient and the element vector of nodal dofs is modified by a constant matrix for patch test fulfilment. Both elements are validated by the generalized individual element patch test [29] and other benchmark problems.

Since DKT4 and RHT4 differ only in the ways they derive the strain-gradient and the elastic energy associated with the strain-gradient is often small compared with that with the strain, their predictions are close especially when the intrinsic material length is small. To the best knowledge of the authors, the proposed elements are probably the first non-mixed/penalty three-dimensional elements which employ only engineering dofs for gradient-elasticity analyses. While the present paper only deals with strain-gradient elasticity, the more general kind of gradient-elasticity in which the elastic energy also depends on rotation-gradient can be accommodated readily [27]. Both DKT4 and RHT4 are coded in Abaqus's UEL user-defined element subroutines which can be requested from the corresponding author.

The methods of interpolation for the previously proposed plane elements have been successfully applied to interpolate the plastic variables in the plane gradient-based plasticicity model [40]. It is hoped that the methods of interpolation for the present 3D elements can equally be applicable to gradient plastic/damage material models [22, 41, 42].

References

1. Tekoglu, C. and P.R. Onck, *Size effects in two-dimensional Voronoi foams: A comparison between generalized continua and discrete models.* Journal of the Mechanics and Physics of Solids, 2008. **56**(12): p. 3541-3564.
2. Aifantis, E.C. *Exploring the applicability of gradient elasticity to certain micro/nano reliability problems.* in *MicroNanoReliability 2007.* 2009. Springer Verlag.
3. Lakes, R., *Experimental methods for study of Cosserat elastic solids and other generalized elastic continua.* Continuum models for materials with microstructure, 1995: p. 1-25.
4. Yang, J.F.C. and R.S. Lakes, *Experimental study of micropolar and couple stress elasticity in compact bone in bending.* Journal of Biomechanics, 1982. **15**(2): p. 91-98.
5. Réthoré, J., et al., *Gradient-elasticity for honeycomb materials: Validation and identification from full-field measurements.* International Journal of Solids and Structures, 2015. **72**: p. 108-117.
6. Lam, D.C.C., et al., *Experiments and theory in strain gradient elasticity.* Journal of the Mechanics and Physics of Solids, 2003. **51**(8): p. 1477-1508.
7. Salehipour, H., A. Shahidi, and H. Nahvi, *Modified nonlocal elasticity theory for functionally graded materials.* International Journal of Engineering Science, 2015. **90**: p. 44-57.
8. Yang, F., et al., *Couple stress based strain gradient theory for elasticity.* International Journal of Solids and Structures, 2002. **39**(10): p. 2731-2743.
9. Sukumar, N. and B. Moran, *C1 natural neighbor interpolant for partial differential equations.* Numerical Methods for Partial Differential Equations, 1999. **15**(4): p. 417-447.
10. Makvandi, R., et al., *Isogeometric analysis of first and second strain gradient elasticity.* Computational Mechanics, 2017: p. 1-13.

11. Kolo, I., H. Askes, and R. de Borst, *Convergence analysis of Laplacian-based gradient elasticity in an isogeometric framework.* Finite Elements in Analysis and Design, 2017. **135**: p. 56-67.

12. Khakalo, S. and J. Niiranen, *Isogeometric analysis of higher-order gradient elasticity by user elements of a commercial finite element software.* CAD Computer Aided Design, 2017. **82**: p. 154-169.

13. Askes, H. and E.C. Aifantis, *Numerical modeling of size effects with gradient elasticity-formulation, meshless discretization and examples.* International Journal of Fracture, 2002. **117**(4): p. 347-358.

14. Tang, Z., S. Shen, and S. Atluri, *Analysis of materials with strain-gradient effects: A meshless local Petrov-Galerkin (MLPG) approach, with nodal displacements only.* Computer Modeling in Engineering and Sciences, 2003. **4**(1): p. 177-196.

15. Sansour, C. and S. Skatulla, *A strain gradient generalized continuum approach for modelling elastic scale effects.* Computer methods in applied mechanics and engineering, 2009. **198**(15-16): p. 1401-1412.

16. Polyzos, D., et al., *A boundary element method for solving 2-D and 3-D static gradient elastic problems: Part I: Integral formulation.* Computer methods in applied mechanics and engineering, 2003. **192**(26-27): p. 2845-2873.

17. Tsepoura, K., et al., *A boundary element method for solving 2-D and 3-D static gradient elastic problems: Part II: Numerical implementation.* Computer methods in applied mechanics and engineering, 2003. **192**(26-27): p. 2875-2907.

18. Petera, J. and J.F.T. Pittman, *Isoparametric Hermite elements.* International Journal for Numerical Methods in Engineering, 1994. **37**(20): p. 3489-3519.

19. Papanicolopulos, S.A., A. Zervos, and I. Vardoulakis, *A three-dimensional C1 finite element for gradient elasticity.* International Journal for Numerical Methods in Engineering, 2009. **77**(10): p. 1396-1415.

20. Beheshti, A., *Finite element analysis of plane strain solids in strain-gradient elasticity.* Acta Mechanica, 2017. **228**(10): p. 3543-3559.

21. Hughes Thomas, J.R., *Finite Element Method - Linear Static and Dynamic Finite Element Analysis.* 1987: Prentice Hall.

22. Zervos, A., P. Papanastasiou, and I. Vardoulakis, *A finite element displacement formulation for gradient elastoplasticity.* International Journal for Numerical Methods in Engineering, 2001. **50**(6): p. 1369-1388.

23. Zervos, A., *Finite elements for elasticity with microstructure and gradient elasticity.* International Journal for Numerical Methods in Engineering, 2008. **73**(4): p. 564-595.

24. Zybell, L., et al., *A three-dimensional finite element for gradient elasticity based on a mixed-type formulation.* 2012. **52**(1): p. 268-273.

25. Zhao, J., W.J. Chen, and S.H. Lo, *A refined nonconforming quadrilateral element for couple stress/strain gradient elasticity.* International Journal for Numerical Methods in Engineering, 2011. **85**(3): p. 269-288.

26. Chen, W.J. and Y.K. Cheung, *Refined non-conforming quadrilateral thin plate bending element.* International Journal for Numerical Methods in Engineering, 1997. **40**(21): p. 3919-3935.

27. Sze, K. and Z. Wu, *Twenty‐four−DOF four‐node quadrilateral elements for gradient elasticity.* International Journal for Numerical Methods in Engineering, 2019. **119**(2): p. 128-149.

28. Xu, M., I.M. Gitman, and H. Askes, *A gradient-enriched continuum model for magneto-elastic coupling: Formulation, finite element implementation and in-plane problems.* Computers and Structures, 2019. **212**: p. 275-288.

29. Felippa, C.A., B. Haugen, and C. Militello, *From the individual element test to finite element templates: evolution of the patch test.* International Journal for Numerical Methods in Engineering, 1995. **38**(2): p. 199-229.

30. Mindlin, R.D. and N.N. Eshel, *On first strain-gradient theories in linear elasticity.* International Journal of Solids and Structures, 1968. **4**(1): p. 109-124.

31. Batoz, J.L. and P. Lardeur, *Discrete shear triangular nine D.O.F. element for the analysis of thick to very thin plates.* International Journal for Numerical Methods in Engineering, 1989. **28**(3): p. 533-560.

32. Batoz, J.L., C.L. Zheng, and F. Hammadi, *Formulation and evaluation of new triangular, quadrilateral,pentagonal and hexagonal discrete Kirchhoff plate/shell ele ments.* International Journal for Numerical Methods in Engineering, 2001. **52**(5-6): p. 615-630.

33. Razaqpur, A.G., M. Nofal, and A. Vasilescu, *An improved quadrilateral finite element for analysis of thin plates.* Finite Elements in Analysis and Design, 2003. **40**(1): p. 1-23.

34. Bergan, P.G. and L. Hanssen, *A new approach for deriving "good" finite elements*, in *The Mathematics of Finite Elements and Applications*, J.R. Whiteman, Editor. 1976, Academic Press London. p. 483-798.

35. Pian, T.H.H. and P. Tong, *Basis of finite element methods for solid continua.* International Journal for Numerical Methods in Engineering, 1969. **1**(1): p. 3-28.

36. Cheung, Y.K. and W.J. Chen, *Refined nine-parameter triangular thin plate bending element by using refined direct stiffness method.* International Journal for Numerical Methods in Engineering, 1995. **38**(2): p. 283-298.

37. Soh, A.-K. and W.J. Chen, *Finite element formulations of strain gradient theory for microstructures and the C0-1 patch test.* International Journal for Numerical Methods in Engineering, 2004. **61**(3): p. 433-454.

38. Khakalo, S. and J. Niiranen, *Gradient-elastic stress analysis near cylindrical holes in a plane under bi-axial tension fields.* International Journal of Solids and Structures, 2017. **110-111**: p. 351-366.

39. Hazen and G. Alan, *Stress concentration around spherical cavities in strain-gradient dependent elastic bodies subjected to uniaxial tension.* 1966, PENNSYLVANIA STATE UNIVERSITY

40. Z.H.Wu, Y.X.Zhou, and K.Y.Sze, *Gradient-plasticity analysis using simple incompatible C1 plane finite element models.* In preparation.

41. De Borst, R. and J. Pamin, *Some novel developments in finite element procedures for gradient‐dependent plasticity.* International Journal for Numerical Methods in Engineering, 1996. **39**(14): p. 2477-2505.

42. Askes, H., J. Pamin, and R. De Borst, *Dispersion analysis and element-free Galerkin solutions of second- and fourth-order gradient-enhanced damage models.* International Journal for Numerical Methods in Engineering, 2000. **49**(6): p. 811-832.